Master Thesis

Optical Transition of Electron in Graphene by Near-Field

Fenda Rizky Pratama

Department of Physics, Graduate School of Science
Tohoku University

July 2018

Acknowledgments

I would like to use this opportunity to acknowledge all people whose direct supports has enable me to finish my master course and this thesis. First of all, I express my sincere gratitude to Prof. R. Saito for his tutelage and guidance which are generously extended beyond physics discussions and academic matters: he motivates me to improve my communication and presentation skills, and his care even help me through various problems of daily life. I am extremely indebted to Mr. M. Shoufie Ukhtary as my tutor and closest friend for this last two years, who always help me to overcome many difficulties I encountered during my research time. All of his kindness will leave lasting memories in my life. I thank to Prof. A.R.T. Nugraha and Dr. E.H. Hasdeo as the other Indonesian countrymen in this group for various technical aids. For other fellow group members: Prof. W. Izumida, Mr. T. Shirakura, Dr. Y. Tatsumi, Mr. K. Ghalamkari, Mr. Md. S. Islam, Mr. N.T. Hung, Mr. Y. Iwasaki, Mr. D. Sato, Mr. T. Shirosaki, it is great to share the time in this group with all of your comradeship. I am grateful to Ms. J. Sasaki, Ms. Y. Wako, Ms. N. Yamamoto, and Ms. M. Sato as the secretaries of the laboratory for helping me to prepare many administrative documents, some of which are indispensable for my survival in Japan. Other than above mentioned people, I also thank Mr. S. Aji who occasionally invite me to divert my mind for a while whenever I need a break, to fellow IGPAS 2018 physics student Mr. B. Aryal for his sincere friendship, and to my counselor Ms. N. Kojima who make me possible to pass turbulent episodes in some of the lowest points in my life. I hope my master graduation will provide a small happiness for my mother and my sister in Indonesia.

Last but not least, I address my gratitude to Tohoku University and Japanese Goverment (MEXT) for providing me a great experience of being a graduate student of Tohoku University as well as the scholarship for the continuity of my study.

Contents

Chapter 1

Introduction

1.1 Purpose of the study

Raman scattering is a powerful technique to investigate physical properties of graphene and the related systems such as few-layers graphene and graphene nano-ribbons [1, 2, 3]. The phenomena arise from the interactions and interplays between electron, photon, and phonon in these materials enable scientists to probe and characterize various properties, among others: the edge type, defect, disorder, strain, and number of layers in system [1, 2, 3, 4, 5]. In the tip-enhanced Raman spectroscopy (TERS), a nanoscale metallic tip of a scanning probe microscopy device is placed few nanometers above the sample, in which the Raman signal is enhanced due to the stong localization of electric field in the vicinity of the tip, known as near-field enhancement [6, 7, 8, 9]. The application of TERS on graphene combines the versatility of Raman spectroscopy with the capability to obtain high spatial resolution beyond diffraction limit [10, 11, 12]. Some efforts to provide quantitative descriptions of TERS as the function of tip near-field enhancement, tip distance and orientation relative to the sample plane of 2D systems in general and graphene in particular have been available in references [13] and [10], respectively. However, the properties of optical transition of electron in graphene affected by near-field from the tip is not yet investigated even though the theoretical analysis is essential for explaining the observed Raman spectra of graphene TERS. **The purpose of this study** is to investigate the effect of electric near-field localization and enhancement in the vicinity of tip on the optical transition of electron

in graphene as well as to understand the origin of the the enhanced Raman spectra in TERS of graphene.

1.2 Organization of the Thesis

This master thesis is organized as follows. The remaining part of Chapter 1 provides the background for the thesis. In Chapter 2, the calculation methods of near-field enhancements in nanoparticles are presented along the electron-photon matrix element which describes light-matter interactions in graphene. The calculation of near-field enhancement around the metallic tips of various size and shape is given Chapter 3, continued by the discussion on the near-field enhancement effect on the electron-near-field matrix element of monolayer graphene in Chapter 4. Finally, in Chapter 5 we conclude the results obtained in the thesis.

1.3 Background

Here some basic concepts to understand this thesis are presented.

1.3.1 Far- and Near- Electromagnetic Fields

The optical responses of material irradiated by visible light such as scattering and absorption are generally obtained by solving the Maxwell Equations for the corresponding system. For any homogenous material with simple shapes e.g. sphere and cyllinder whose size is comparable to the wavelength of light λ, the analytical treatment of this scattering problem is known as the Mie theory [6, 14]. Based on the distance from the material, the total electromagnetic fields (summation of incoming and scattered fields) consist of two terms: the far-field and near-field. Far-field is defined as the propagating field at distance significantly large from the material, in contrast to the near-field which is defined as the localized field in the vicinity of the material [6].

To illustrate spatial dependences of the properties of electromagnetic fields, let us consider the case of an oscillating electric-dipole which radiates electromagnetic wave with wave vector $k = \frac{2\pi}{\lambda}$. The dipole is placed in a homogenous medium whose relative permittivity ϵ_m. The corresponding magnetic field $\mathbf{H}$ and electric field $\mathbf{E}$ can

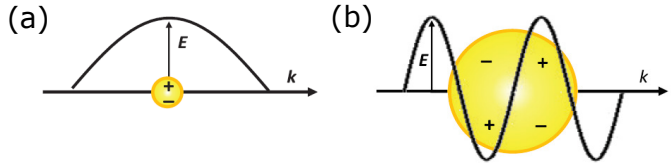

Figure 1.1 Illustration for LSP mechanism in metallic nano-sphere when its size is (a) much smaller (b) comparable to or larger than the wavelength of the excitation [17][1].

be written as [15, 16]:

$$\mathbf{H} = \frac{ck^2}{4\pi}(\hat{\mathbf{r}} \times \mathbf{p})\frac{e^{ikr}}{r}\left(1 - \frac{1}{ikr}\right); \tag{1.1}$$

$$\mathbf{E} = \frac{1}{4\pi\epsilon_m\epsilon_0}\left(k^2(\hat{\mathbf{r}} \times \mathbf{p}) \times \hat{\mathbf{r}}\frac{e^{ikr}}{r} + [3\hat{\mathbf{r}}(\hat{\mathbf{r}} \cdot \mathbf{p}) - \mathbf{p}]\left[\frac{1}{r^3} - \frac{ik}{r^2}\right]e^{ikr}\right), \tag{1.2}$$

where $\mathbf{p}$ and $\hat{\mathbf{r}}$ are dipole moment and unit vector in the direction of particular point P, respectively, and r is the distance from the origin to P. In the far-field zone defined as $kr \gg 1$, the terms $\propto \frac{1}{r}$ is much larger than the rest terms, therefore Eqs. (1.1) and (1.2) are expressed as follows [16]:

$$\mathbf{H} = \frac{ck^2}{4\pi}(\hat{\mathbf{r}} \times \mathbf{p})\frac{e^{ikr}}{r}; \tag{1.3}$$

$$\mathbf{E} = \sqrt{\frac{\mu_0}{\epsilon_m\epsilon_0}}(\mathbf{H} \times \hat{\mathbf{r}}), \tag{1.4}$$

while in the near-field zone, i.e. $kr \ll 1$, we can select the dominating terms $\propto \frac{1}{r^2}$ and $\propto \frac{1}{r^3}$ from Eqs. (1.1) and (1.2), which reduce to [16]:

$$\mathbf{H} = \frac{ick}{4\pi}(\hat{\mathbf{r}} \times \mathbf{p})\frac{1}{r^2}; \tag{1.5}$$

$$\mathbf{E} = \frac{1}{4\pi\epsilon_m\epsilon_0 r^3}[3\hat{\mathbf{r}}(\hat{\mathbf{r}} \cdot \mathbf{p}) - \mathbf{p}]. \tag{1.6}$$

Eqs. (1.5) and (1.6) show that in the near-field zone the electric field is predominant, since the magnitude of magnetic field is small and ultimately vanishes in the static case, i.e. $kr \to 0$ [16]. It is also concluded that the electric near-field does not propagate since it does not consists of the propagation term e^{ikr}, and quickly decays as the distance r increases because its dependence to the factor $\frac{1}{r^3}$. The near-field localization and enhancement around nanoparticles and nano-tips as response of irradiating light is discussed in the next Sub-chapter.

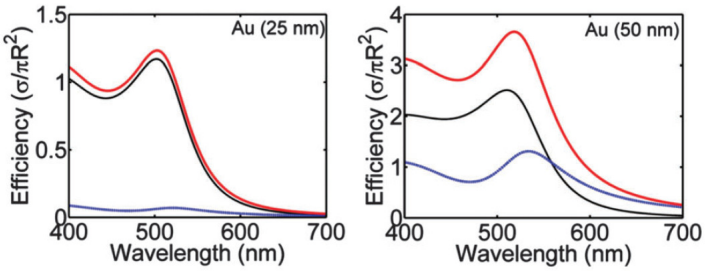

Figure 1.2 Mie theory calculations of the extinction (red), scattering (blue) and absorption (black) of the Au spherical nanoparticle of radius 25 nm (left) and 50 nm (right) [23].

1.3.2 Near-Field Enhancement in Nanostructures

Metallic nanostructures whose spatial dimensions are significantly smaller than the wavelength of irradiating light such as nanoparticles and nano-tips have been studied with special interest in the fields of nano-optics and plasmonics, since they exhibit a prominent effect, namely electric near-field enhancement compared with the incident light in their vicinity [6, 18, 16, 19, 20]. One of the mechanism responsible for this phenomenon is that the oscillation of electric field from the incoming electromagnetic wave periodically displaces free electrons cloud from the surface of the metallic nanostructure along polarization direction of the electric field, which in return generates a localized response field with a greater magnitude compared with irradiating light [21, 17, 22]. The phenomenon of the electric field-driven electron oscillation in metallic nanostructures is also termed as the **localized surface plasmon (LSP)**.

In Fig. 1.1, we illustrate LSP mechanism for the case of spherical nanoparticle. When the radius of sphere is much smaller than wavelength of the light, electric field is distributed uniformly along the particle and therefore the electron cloud oscillates coherently, resulting the dipole excitation [21, 17] as shown in (a). However, in the case when the size of nanoparticle is comparable to or larger than wavelength of the light, the distribution of the electric field in nanoparticle is no longer uniform and thus the electron cloud oscillates incoherently, which generates higher order excitations, e.g. quadrupole and octopole excitations [21, 17], as given in (b). The dipole and higher-modes excitations in the spherical nanoparticle will be discussed more thoroughly in Chapter 2.

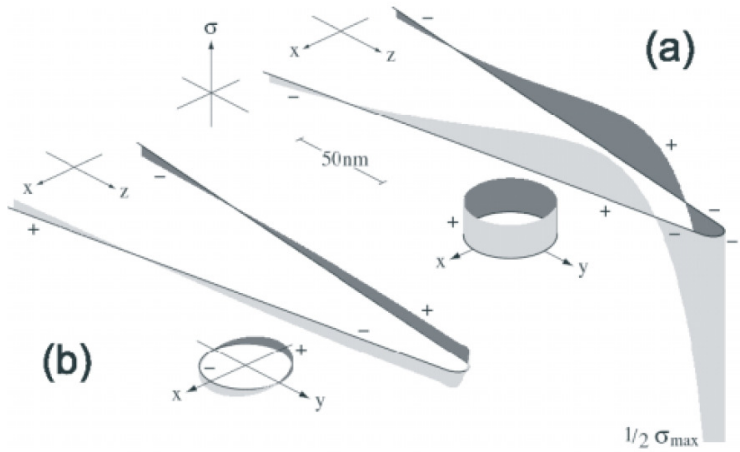

Figure 1.3 Induced charge density (σ) for the case of electric field is polarized (a) parallel and (b) perpendicular to the tip axis [7].

The near-field enhancements around nanoparticles are usually calculated in the terms of a variable termed extinction cross section. Extinction cross section σ_{ext} is expressed as the summation of the scattering and absorption cross sections, σ_{sca} and σ_{abs}. For the small spherical nanoparticle of radius a and relative permittivity $\epsilon_r = \epsilon_1 + i\epsilon_2$ surrounded by medium whose dielectric constant is $\epsilon_0\epsilon_m$, the cross sections are mathematically given as follows [23]:

$$\sigma_{\text{sca}} = \frac{24\pi^3 v^2 \epsilon_m}{\lambda^4} \frac{(\epsilon_1 - \epsilon_m)^2 + {\epsilon_2}^2}{(\epsilon_1 + 2\epsilon_m) + {\epsilon_2}^2}, \tag{1.7}$$

$$\sigma_{\text{abs}} = \frac{18\pi v {\epsilon_m}^{3/2}}{\lambda} \frac{\epsilon_2}{(\epsilon_1 + 2\epsilon_m) + {\epsilon_2}^2}, \tag{1.8}$$

$$\sigma_{\text{ext}} = \sigma_{\text{sca}} + \sigma_{\text{abs}}, \tag{1.9}$$

where $\lambda \gg a$ is the wavelength of the light and v is the volume of individual nanoparticle. An example of the Mie theory calculations on the wavelength dependence of extinction cross section for the individual Au spherical nanoparticle is given by the Fig. 1.2, in which the peaks are observed in the range of λ=500-550 nm. In the Chapter 2, we shall show that the cross sections are closely related to the near-field enhancements inside and outside nanoparticle, that is, if the three cross-sections are high, so are the near-field enhancements.

In the case of metallic nano-tip, other than LSP, accumulation of electric charge in

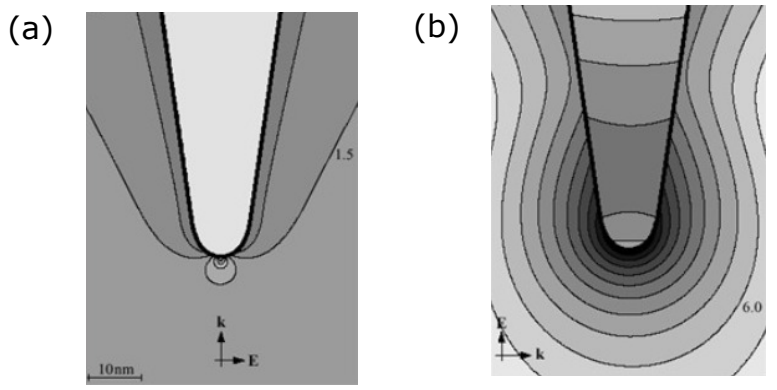

Figure 1.4 Calculation of the near-field in vicinity of Au tip of 5 nm radius in water irradiated by monochromatic waves with $\lambda = 810$ nm, for electric field polarizations (a) perpendicular and (b) parallel relative to the tip's axis . The successive lines of the E^2 countour in the figure differs by factor 2. The near-field in (b) is almost rotationally symmetric in the vicinity of the tip [18].

the sharp end of tip (tip apex) is the main factor which contributes to the near-field enhancement in its vicinity [7]. The phenomenon of charge accumulation associated with the sharpness in nanostructure geometry is called **electrostatic lightning-rod effect** [24, 20]. In Fig. 1.3 we illustrate induced surface charge density in the vicinity of metallic tip for two different electric field polarizations of incoming light, which shows large (small) charge accumulation as the electric field is polarized parallel (perpendicular) to the tip axis. Consequently, maximum near-field enhancement is obtained when the electric field is polarized parallel to the axis, otherwise the enhancement is significantly weaker [22, 24]. In Fig. 1.4 we show the contrasting difference of near-field enhancements for the two considered cases, i.e. when the electric field polarizations of radiating light are perpendicular and parallel relative to the tip axis, from which it is inferred that near-field enhancement for the parallel polarization is much larger compared to the perpendicular polarization.

The magnitude of near-field enhancement factor, of which in this work is defined as the absolute value of ratio between induced near-field $\mathbf{E}$ and incident field from light $\mathbf{E}_0$, $|\mathbf{E}/\mathbf{E}_0|$, is largely depends on the material of nano-tip as well as the wavelength of incident light. In Fig. 1.5 we depict two instances of the calculated near-field enhancement around metallic nano-tips made of two different materials. In (a), Pt nanotips is irradiated by an electromagnetic wave of wavelength of 808 nm, while in

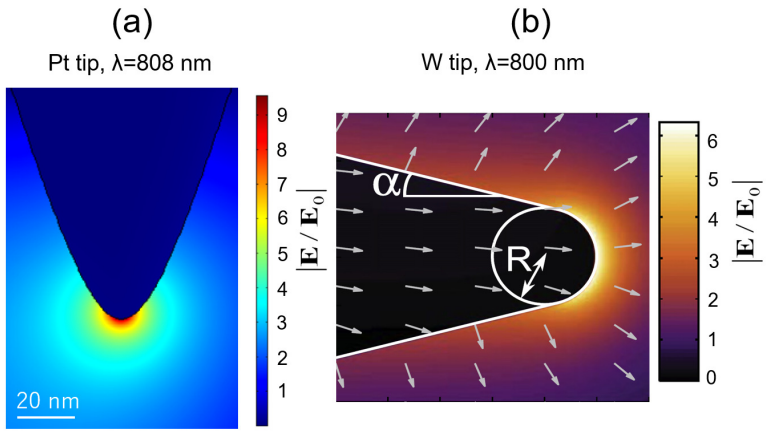

Figure 1.5 Near-field enhancement in the vicinity of (a) Pt tip irraddiated by the light of wavelength 808 nm [25], and (b) W tip illuminated by light of wavelength 800 nm [26]. In each case the nano-tips are placed in vacuum and the polarization direction of electric field is perpendicular to the tip axis.

(b), a conical W tip of radius R=10 nm and opening angle α=15 degree is illuminated by light whose wavelength is 800 nm. The magnitude of near-field enhancements in (a) and (b) are around 9.55 and 6.2, respectively. Near-field enhancement from Au nano-tips as the function of its geometrical parameters and the wavelength of illuminating light shall be discussed in Chapter 3, along with the reproduction of calculated results depicted in Fig. 1.5.

1.3.3 Brief Review on Graphene

We briefly review some properties of graphene because the main subject of this work is the near-field effect on the optical transition in the corresponding material. Graphene is a single-atom thick material in which carbon atoms are arranged in two-dimensional hexagonal honeycomb lattice. Since its isolation and characterization by Novoselov et al. in 2004 [27], graphene has emerged to become a mainstream research topic in the field of condensed-matter physics and material science due to its unique physical properties and the promising technological applications [28]. Some examples of these properties including very high electrical conductivity, tremendous mechanical strength, and the linear electronic energy dispersion where the effective mass of the electron becomes zero [29, 30, 31, 32].

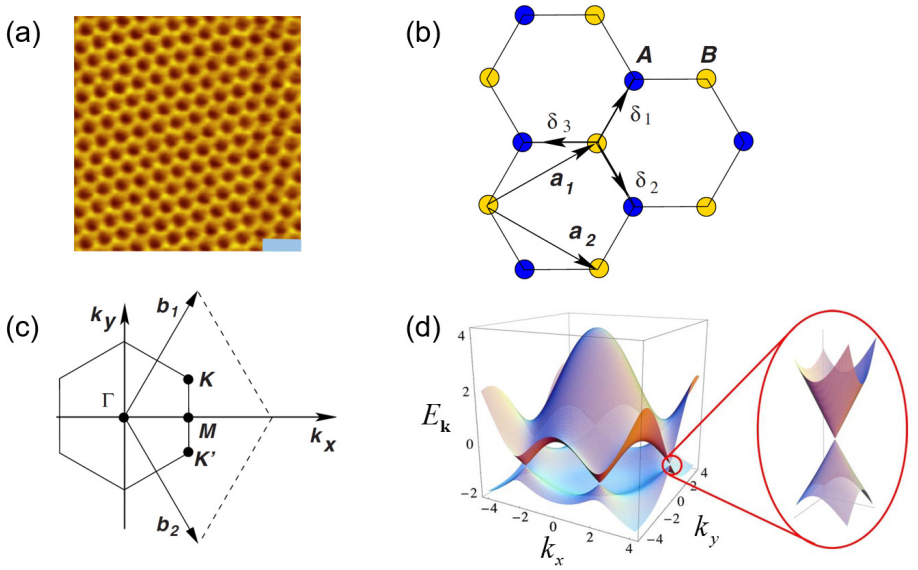

Figure 1.6 (a) STM image of graphene on graphite substrate. The length of blue scale bar is 500 pm [32]. (b) The unit cell and (c) Brillouin zone, and (d) Electronic energy dispersion of graphene. Zoom: the Dirac cone around K point [31].

The scanning tunneling microscopy (STM) image of graphene on graphite substrate with atomic resolution is presented in Fig. 1.6(a). The unit cell of graphene which consists of two atoms A and B is given in (b). The unit vectors in the real space are $\mathbf{a}_1 = \frac{a}{2}(3, \sqrt{3})$ and $\mathbf{a}_2 = \frac{a}{2}(3, -\sqrt{3})$, where $a = \mid \mathbf{a}_1 \mid = \mid \mathbf{a}_1 \mid = 2.46$ Å and $a_{CC} \approx 1.42$ Å is the length of nearest-neighbor vectors $\boldsymbol{\delta}_1$, $\boldsymbol{\delta}_2$, and $\boldsymbol{\delta}_3$ [31]. In (c), we depict the Brillouin zone of graphene showing high symmetry points Γ, M, and K. The reprocical lattice vectors of graphene are $\mathbf{b}_1 = \frac{2\pi}{3a}(1, \sqrt{3})$ and $\mathbf{b}_2 = \frac{2\pi}{3a}(1, -\sqrt{3})$ [31]. The tight-binding electronic energy dispersion of graphene is shown in (d). The region around K and K' points in the Brillouin zone where the electronic energy is a linear function of wave vector is known as the **Dirac cone**. In this region electron behaves as a massless relativistic particle traveling with speed about 300 times smaller than the speed of light [30, 31].

In Chapter 4, we employ the tight-binding graphene wave function to calculate the electron interaction with the near-field scattered from Au nano-tip irradiated by the visible light. The interaction determines the properties of electron optical transition and absorption in graphene.

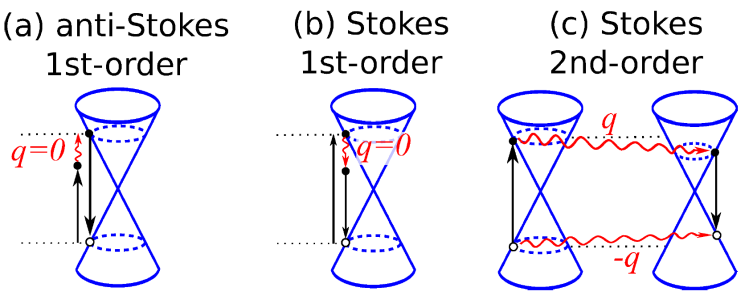

Figure 1.7 Raman processes: (a) first-order anti-Stokes, (b) first- (c) second-order Stokes process. Straight and wiggly lines indicate electron-photon and electron-phonon interactions, respectively [33].

1.3.4 Raman Spectroscopy of Graphene

Along with graphite and carbon nanotubes, graphene forms a family of carbon materials sharing similar characteristic of possessing sp^2 orbital [34]. Monolayer graphene is the simplest structure of these materials, thus it becomes a perfect prototype material to study the properties of sp^2 carbon family [34]. The most superior characterization tool of sp^2 carbon allotropes in the terms of both simplicity and versatility is provided by Raman spectroscopy [1], which is based on the inelastic scattering of visible light through interactions involving electrons and phonons in materials, known as **Raman scattering or Raman effect**. The Raman shift $\Delta\omega$, which is defined as the difference between frequency of incident light (ω_i) and scattered light (ω_s), $\Delta\omega = \omega_i - \omega_s$ can be positive or negative, the former (later) is known as Stokes (anti-Stokes) process. Generally, anti-Stokes signal is weaker than the Stokes signal, and therefore usually only Stokes signal is considered in Raman characterization [34]. In graphene, Raman scattering process involves the electron-photon and electron-phonon interactions, described as follows: 1) electron from valence band undergoes optical transition to the conduction band by absorbing photon, followed by 2) creation of phonon(s), and finally 3) electron is de-excited to its initial state by emitting photon. In the first-order Raman scattering momentum of the emitted phonon is zero ($q = 0$), while phonon with non-zero momentum ($q \neq 0$) is emitted in the second-order Raman scattering, as schematically depicted in Fig. 1.7.

A comparison of Raman spectra of graphene with several other sp^2 carbon allotropes is presented in Fig. 1.8. The Raman signature of sp^2 carbon allotropes is

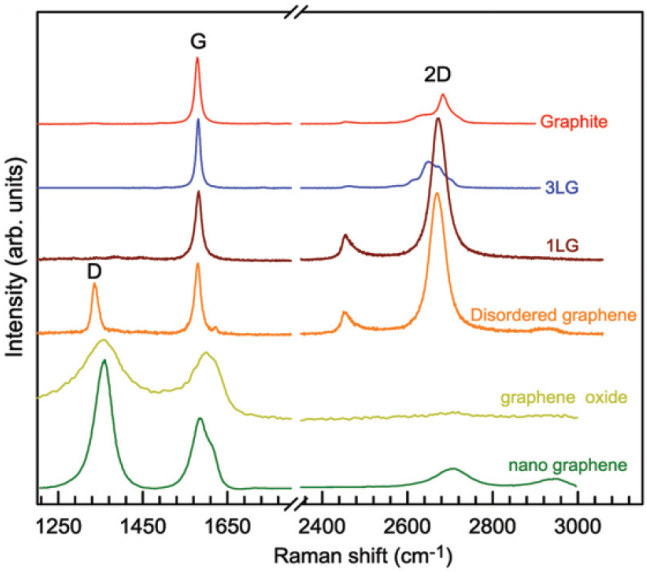

Figure 1.8 Raman spectra of graphite, three-layers graphene (3LG), monolayer graphene (1LG), disordered graphene, graphene oxide, and nano graphene [35].

G-band peak at Raman shift of $\sim$1580cm^{-1}, which is attributed to the first-order Raman scattering [34]. The second order Raman scattering gives rise to the G'-band peak ($\sim$2700cm^{-1}), while D-band peak ($\sim$1350cm^{-1}1) is only observed in the presence of defect in the structure [34]. It is noteworthy that the Raman shift of G' peak is approximately twice of the D peak, and for this reason some authors label the former peak as 2D band [5]. In Chapter 2, quantum description of how electron in graphene interacts with photon is described with time-dependent perturbation theory.

1.3.5 Tip-Enhanced Raman Spectroscopy of Graphene

Tip-enhanced Raman spectroscopy (TERS) is one of the novel technique to characterize materials, and have been extensively applied to study sp^2 carbons including graphene [11, 36, 37, 38], carbon nanotubes [7], graphene nanoribbons [39], and C-60 [40]. In the experimental set-up of TERS, a metallic nano-tip of scanning probe microscopy device is placed near the sample of the characterized material to achieve two goals: 1) to obtain high spatial resolution beyond diffraction limit, and 2) to enhance the Raman signal in the near-field regime [7].

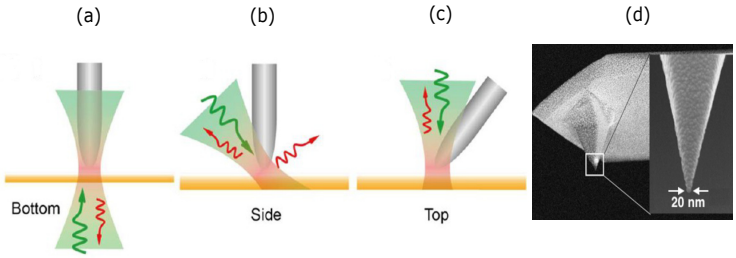

Figure 1.9 (a) Bottom, (b) side, and (c) top illuminations geometry in TERS. The green and red wiggly arrows illustrate incoming and scattered Raman signals, respectively [8]. (d) SEM image of Ag-coated Si AFM tip. The size of the tip is 20 nm [9].

Fig. 1.9(a)-(c) shows some common configurations of TERS based on the direction of incoming light relative to the positions of the sample and tip, i.e. bottom, side, and top illuminations. The three configurations can be applied in TERS that is based on atomic force microscopy (AFM), while in the scanning-tunneling microscopy (SEM)-based TERS, side illumination (b) is often used [9]. Side illumination produces large near-field enhancement around the tip using p-polarized light compared to the bottom illumination geometry (a) [8]. This fact is consistent to the polarization dependence of near-field enhancement around the tip as previously discussed. An instance of SEM image of Ag-coated Si AFM tip is given in (d). The tip used in TERS is usually cone-shaped with the radius of curvature around 10 to 30 nm at tip apex [8], and can be fabricated economically by electrochemical etching [41]. In Chapter 3, we shall show that the enhancement is also determined by the shape of the tip other than its radius of curvature.

Here we present an instance of TERS measurement of monolayer graphene using Au-coated tip and excitation wavelength 532 nm in the top illumination geometry. The effect of the tip on the Raman spectrum of graphene is given by Fig. 1.10(a), showing the enhancement of D, G, and 2D bands intensity when the tip is approached to the sample. The confirmation of the signal enhancement is in (b), which depicts the substraction of the Raman spectra acquired when the tip is approached and rectracted.

In chapter 4, we present a microscopic picture based on time-dependent perturbation theory to explain of how the near-field around the tip enhances the optical matrix element, which is a variable describing the coupling of electromagnetic field with the electron.

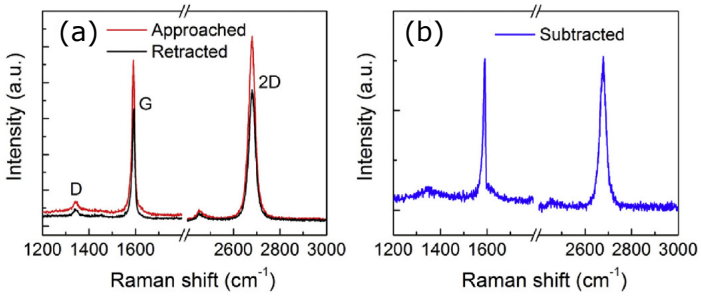

Figure 1.10 (a) The monolayer graphene's Raman spectra measured when the tip is approached and retracted (b) The subtraction of Raman spectrum given in (a) [37].

1.3.6 Coupling Between Near-Field and Electron in Graphene

Here we review a recent progress on the theoretical work on the coupling between near-field and electron in graphene, because we shall shows that the corresponding work seems to confirm the results obtained independently in this thesis in around the same time. Very recently, Mueller and Reich [42] provide a microscopic theory of optical absorption in graphene enhanced by square lattices of plasmonic nanoparticles. By employing the tight-binding graphene wave function, they analytically calculate the interaction of graphene with the electrostatic potential of an individual nanoparticle $\phi_{\mathrm{pl}}(\mathbf{r})$ by the electron-plasmon matrix element $M_{\mathrm{el-pl}}$ [42]:

$$M_{\mathrm{el-pl}} = -\frac{e}{2}\langle \Psi^{\mathrm{c}}(\mathbf{k}_{\mathrm{c}})|\phi_{\mathrm{pl}}(\mathbf{r})|\Psi^{\mathrm{v}}(\mathbf{k}_{\mathrm{v}})\rangle, \tag{1.10}$$

where $\mathbf{k}$ is electron wave vector and e is the elementary charge, while indices v and c indicate the valence and conduction band, respectively. Because of the periodicity the nanoparticles, they are able to extract the Fourier components of the electron-plasmon matrix element, and show that the near-field induces the non-vertical optical transition in the electron, which indicate the change of electron wave vector in the transition from valence to conduction bands as illustrated by Fig. 1.11(a). In their work, the change of electron wave vector are discrete, given by [42]:

$$\mathbf{k}_{\mathrm{c}} - \mathbf{k}_{\mathrm{v}} = (\Delta\mathbf{k}_x, \Delta\mathbf{k}_y) = \frac{2\pi}{\Delta R}(m_x, m_y),\ m_x, m_y \in \mathbb{Z}, \tag{1.11}$$

where ΔR is the spacing distance between nanoparticles. They also show that the nodes of electron-plasmon is determined by its wave vector change in the Brillouin

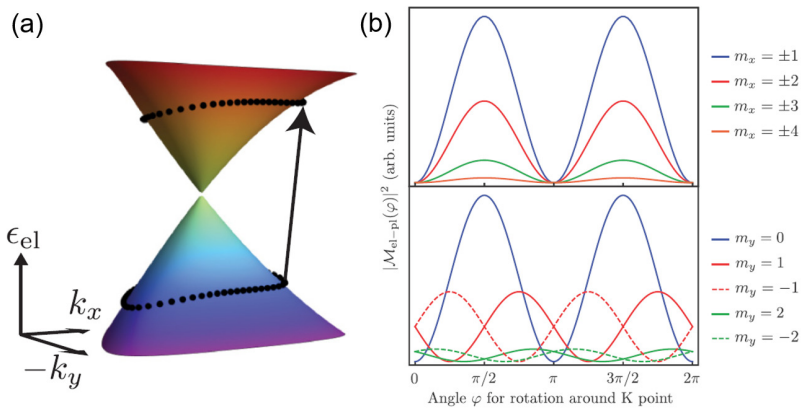

Figure 1.11 (a) Sketch of non-vertical optical transition of electron in graphene (b) Electron-plasmon matrix element around K point. Top: for several m_x and m_y=0. Bottom: for several m_y and m_x=1 [42].

zone, as given in (b). In the Chapter 4, by employing a rather different theoretical approach, we argue that localized near-field from the tip which is non-periodic, also implies non-vertical optical transition of electron in graphene. The effect of the change of electron wave vector is then observed as nodes in the absorption spectra.

Chapter 2

Methods

2.1 The Optical Properties of Noble Metals

2.1.1 Drude and Drude-Lorentz Models

The optical properties of materials depend on the response of the electrons by their interaction with radiating light. Understanding the properties are essential to explain why noble metals such as Au and Ag are mainly utilized in the context where the plasmonic effects are one of the primary interests, e.g. in the near-field spectroscopy. The mathematical descriptions of how electrons in the materials interact with the electric field of electromagnetic waves are provided by two well-known models: 1) the Drude model for free electrons, and 2) the Drude-Lorentz model for the case in which electrons are restricted by an internal restoring force. Although these models only give the picture of the interactions in a simplified system, they present some insightful accounts on optical properties of the real materials.

The electrically neutral system of electron gas and the positive ions is called plasma. In the **Drude model**, metals or doped semiconductors are regarded as plasma where the valence electrons freely move around the positive ion cores [43]. In such materials, the presence of an electromagnetic wave induces the oscillation an electron which experiences no restoring force. The Equation of motion of the electron is given as follows:

$$m_e \frac{\mathrm{d}^2\mathbf{x}(t)}{\mathrm{d}t^2} + m_e\Gamma\frac{\mathrm{d}\mathbf{x}(t)}{\mathrm{d}t} = -e\mathbf{E}(t), \tag{2.1}$$

where $\mathbf{x}(t)$ and m_e are the displacement and effective mass of electron, respectively. To provide more realistic description of the electrons in metals and semiconductors, it is assumed that the effective mass m_e incorporates some aspects of the band structure [16]. The first and second terms of in the left-hand side of the Eq. (2.1) correspondingly represent forces from an accelerated electron and damping of the medium proportional to a constant Γ, which is interpreted as the inverse of the averanged collision time between electron and the positive ion cores (also called relaxation time) τ, i.e. $\Gamma = \frac{1}{\tau}$. For the electron gas in the room temperature, τ is approximately in order of 10^{-14} s, which corresponds to Γ =100 THz [16, 43]. By regarding that the displacement is time-harmonic, that is $\mathbf{x}(t) = \mathbf{x}_0 e^{-i\omega t}$ with ω being frequency of the electromagnetic wave, thus Eq. (2.1) becomes

$$-\omega^2 \mathbf{x}(t) - i\omega\Gamma\mathbf{x}(t) = \frac{-e\mathbf{E}(t)}{m_e}. \tag{2.2}$$

We can express the displacement $\mathbf{x}(t)$ as a function of electric field $\mathbf{E}(t)$ as

$$\mathbf{x}(t) = \frac{e\mathbf{E}(t)}{m_e}\frac{1}{\omega^2 + i\Gamma\omega}. \tag{2.3}$$

The displacement of N electrons generate the macroscopic polarization

$$\mathbf{P} = -Ne\mathbf{x}, \tag{2.4}$$

which in return contributes to the electric displacement $\mathbf{D}$ given by

$$\mathbf{D} = \epsilon_r\epsilon_0\mathbf{E} = \epsilon_0\mathbf{E} + \mathbf{P}. \tag{2.5}$$

By combining Eqs. (2.3)-(2.5), a simple expression of relative permittivity of electron gas ϵ_r defined by Eq. (2.5) can be written as

$$\epsilon_r(\omega) = 1 - \frac{{\omega_\mathrm{p}}^2}{\omega^2 + i\Gamma\omega}, \tag{2.6}$$

where ω_p is called the plasma frequency, defined by

$$\omega_\mathrm{p} \equiv \left(\frac{Ne^2}{\epsilon_0 m_e}\right)^{\frac{1}{2}}. \tag{2.7}$$

When we write the relative permittivity as the summation of its real and imaginary parts, $\epsilon_r = \epsilon_r^{(1)} + i\epsilon_r^{(2)}$, we get from Eq. (2.6):

$$\epsilon_r^{(1)}(\omega) = 1 - \frac{{\omega_\mathrm{p}}^2}{\omega^2 + \Gamma^2}; \tag{2.8}$$

$$\epsilon_r^{(2)}(\omega) = \frac{{\omega_\mathrm{p}}^2\Gamma}{\omega(\omega^2 + \Gamma^2)}. \tag{2.9}$$

In the lightly-damped system compared with angular frequency ω in which $\omega \gg \Gamma$, the relative permittivity is therefore

$$\epsilon_r(\omega) \approx 1 - \frac{{\omega_\mathrm{p}}^2}{\omega^2}. \tag{2.10}$$

It is informative to compare the relative permittivity ϵ_r with another important physical property of a material affected by a time-varying external electric field, the optical conductivity $\sigma(\omega)$. By expressing the Equation of motion for electron in the term of time-harmonic velocity $\mathbf{v}(t) = \mathbf{v}_0 e^{-i\omega t}$, we have

$$-i\omega\mathbf{v}(t) + \Gamma\mathbf{v}(t) = \frac{-e\mathbf{E}(t)}{m_e}. \tag{2.11}$$

The velocity of electron $\mathbf{v}$ and conductivity σ are related to the current density $\mathbf{J}$ as follows:

$$\mathbf{J} = -Ne\mathbf{v} = \sigma\mathbf{E}. \tag{2.12}$$

By using Eqs. 2.11 and 2.12, the optical conductivity is given by

$$\sigma(\omega) = \frac{Ne^2}{m_e}\frac{1}{\Gamma - i\omega} = \frac{\sigma_0}{1 - i\omega\tau}, \tag{2.13}$$

where $\sigma_0 = \frac{Ne^2\tau}{m_e}$ is definition of the conductivity. By comparing Eqs. (2.6) and (2.13). The relative permittivity ϵ_r can be equivalently expressed as

$$\epsilon_r(\omega) = 1 + i\frac{\sigma(\omega)}{\epsilon_0 m_e}. \tag{2.14}$$

The result from Eq. (2.10) describes the permittivity of free electron gas where $\epsilon_r \to 1$ as the frequency of electromagnetic wave ω becomes much larger than the plasma frequency ω_p. For the noble metals (Au, Ag, Cu, and Pt), a modification on Eq. (2.6) is required in order to describe relative permittivity in the region $\omega > \omega_\mathrm{p}$ where the optical response is dominated by the free s electrons, because highly polarized environment is created by the filled d-band close to the Fermi surface [16]. The background polarization due to the positive in cores $\mathbf{P}_\infty = \epsilon_0(\epsilon_\infty - 1)\mathbf{E}$ should be added into Eq. (2.5). Hence the modified relative permittivity is given by

$$\epsilon_r = \epsilon_\infty - \frac{{\omega_\mathrm{p}}^2}{\omega^2 + i\Gamma\omega}, \tag{2.15}$$

where the value of background polarization ϵ_∞ that can be defined by taking the limit

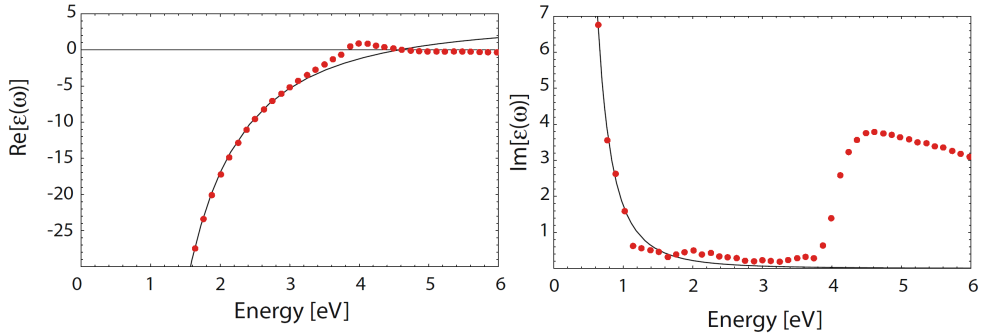

Figure 2.1 Real and imaginary parts of Au relative permittivity from Drude model (solid line) fitted to the experimental data from [44] (dots) [16].

of $\omega \to \infty$ is usually within the range of 1-10 [16]. As for ϵ_∞, the constants Eq. (2.15) are adjusted to the data obtained from an experiment. An instance of this semi-empirical ϵ_r determination for the case of Au is depicted by Fig. 2.1, from which it is inferred that the model already deviates from the experimental result in the boundary between near-infrared and visible regions around 2 eV. For photon energy around 4 eV, which corresponds to the near-ultraviolet regime, a peak appears in the real part of relative permittivity, while sudden increase of value is observed in its imaginary part. These behaviors are attributed to the interband transition of electrons which occurs when the energy of electromagnetic wave is sufficiently high [16], otherwise only intraband transition is possible [45]. Both intraband and interband transitions occur because a radiating electromagnetic wave transfers its energy and momentum to the electron. The optical properties of electron undergoes interband transition can be described by the **Drude-Lorentz model** [16, 46, 47], where the Equation of motion of bound electron is presented as follows:

$$m_e \frac{\mathrm{d}^2\mathbf{x}(t)}{\mathrm{d}t^2} + m_e\Gamma\frac{\mathrm{d}\mathbf{x}(t)}{\mathrm{d}t} + m_e\omega_0^2\mathbf{x}(t) = -e\mathbf{E}(t). \tag{2.16}$$

By the similar mathematical arguments perviously applied to get at Eq. (2.15), the Drude-Lorentz relative permittivity is derived as

$$\epsilon_r^{(\mathrm{L})} = \epsilon_\infty^{(\mathrm{L})} - \frac{N^{(\mathrm{L})}e^2}{m_e^{(\mathrm{L})}\epsilon_0}\frac{1}{(\omega^2-\omega_0^2)+i\Gamma^{(\mathrm{L})}\omega}, \tag{2.17}$$

where the superscript-(L) is added to some constants in order to distinguish from the ones contained in the Drude model. The real and imaginary parts of the Drude-Lorentz

relative permittivity are given by

$$\epsilon_r^{(1)(\mathrm{L})}(\omega) = \epsilon_\infty^{(\mathrm{L})} - \frac{N^{(\mathrm{L})}e^2}{m_e^{(\mathrm{L})}\epsilon_0}\frac{\omega^2-\omega_0^2}{(\omega^2-\omega_0^2)+{\Gamma^{(\mathrm{L})}}^2\omega^2}; \tag{2.18}$$

$$\epsilon_r^{(2)(\mathrm{L})}(\omega) = \frac{N^{(\mathrm{L})}e^2}{m_e^{(\mathrm{L})}\epsilon_0}\frac{\Gamma^{(\mathrm{L})}\omega}{(\omega^2-\omega_0^2)+{\Gamma^{(\mathrm{L})}}^2\omega^2}. \tag{2.19}$$

The result from Eq. (2.19) is a Lorentzian function which is maximum when $\omega = \omega_0$, and consequently the constant ω_0 is regarded as the resonant frequency.

For many purposes, the summation of the Drude and the Drude-Lorentz terms is used as the fitting function to estimate the relative permittivity of noble metals at a particular optical frequency. However, assessing the optical properties of nanomaterials require the modification of both models, because the collision of electrons at surface boundary of nanoparticles which is pronounced in nano-scale regime should be considered. The discussion on size-dependence of relative permittivity is presented in the next sub-section.

2.1.2 Size Effect of the Relative Permittivity

In the the Drude and the Drude-Lorentz models previouly reviewed, it is assumed that in the materials, the travelling electrons constantly scatter only with the backgroud ion cores or other electrons. The averaged time required before the next collision (or relaxation time) τ determines the damping constant Γ by the inverse relation. In more complex systems where defects, phonons, etc. may present, τ should be modified because their presence affects the movement of electron by the additional collisions. The modification of τ which accounts the total collisions of electron with the constituents in material is given by the **Matthiessen rule** [17], written as

$$\frac{1}{\tau} = \frac{1}{\tau_0} + \frac{1}{\tau_\mathrm{d}} + \frac{1}{\tau_\mathrm{ph}} + ..., \tag{2.20}$$

where τ_d and τ_ph are consecutively the relaxation times due to the electron collisions with defect and phonon, while τ_0 is the intrinsic relaxation time in the bulk material. In the nanoscale, the collision of electron with the surface boundary of material must be included especially in the case where the material size is smaller than the mean-free-path of electron (For Au and Ag, the corresponding first-principles calculation values are 37.7 and 53.3 nm, respectively [48]). By using the analogy of Matthiessen

rule, the modified damping constant which includes the electron-surface collision is given by

$$\Gamma = \Gamma_0 + \Gamma_{\rm s}. \tag{2.21}$$

In general, the surface damping constant Γ_s is expressed as a function of Fermi velocity $v_{\rm F}$, effective distance traversed by electron before scattering in the presence of the surface of nano-structure whose length is L, and a dimensionless constant A, as follows [49, 50, 51, 52, 53, 46, 54, 17]:

$$\Gamma_{\rm s} = A\frac{v_F}{L}. \tag{2.22}$$

The obtained value of L varies depending on the theoretical approach [49, 50, 51, 55, 52, 53]. Based on geometric probability calculation, an expression of L applicable to any convex-shaped nanostructure is related to its volume V and surface area S by [50, 46, 17]:

$$L = \frac{4V}{S}. \tag{2.23}$$

For Au nanoparticles, there are several available fitting values of A, which falls in the range of $0 \leqslant A \leqslant 1$ [52, 46, 54] and differs according to the interface between the particle and the surrounding medium [51, ?]. The physical meaning of A is thought to be the fraction of electron-surface scattering events that are totally inelastic [51]. Eqs. (2.21)-(2.23) are therefore applied to account damping coefficient due the electron-surface collision which can not be neglected in nanoscale materials. We choose to use $A = 0.33$ as the best fitting value for an individual Au nanoparticle optical absorption [46], while Fermi velocity $v_{\rm F} = 1.41 \times 10^{15}$nm s^{-1} [55] is employed for any relevant calculation.

In Fig. 2.2, we illustrate the differences between relative permittivity of Au bulk and spherical nanoparticles whose radiuses 20, 10, and 5 nm in the visible region. From the figure, it is inferred that the real part of relative permittivity does not significantly increase with descreasing the radius of nanoparticle, while its imaginary part increases quickly especially for the long wavelength regime. We shall show later that one of the required conditions of the occurence of plasmonic resonance in small nanoparticle is zero imaginary part of relative permittivity, which is macroscopically related to the enhanced optical absorption [43].

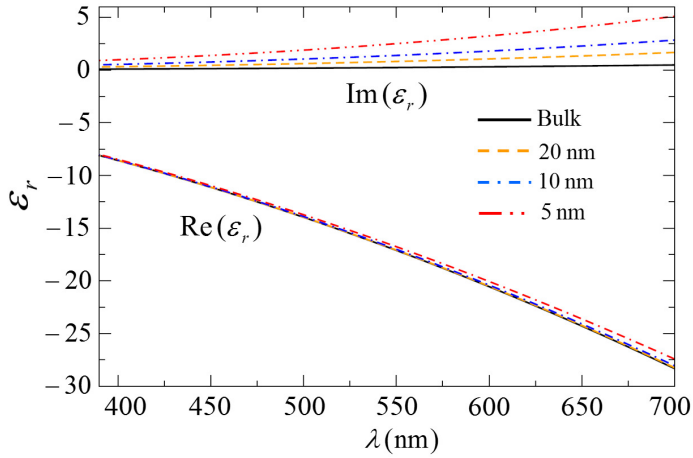

Figure 2.2 Calculated relative permittivity of Au bulk and spherical nanoparticles of radius 20, 10, and 5 nm. The Drude fitting parameters are adapted from reference [56] .

2.2 Electromagnetics within the Quasi-static Approximation

Electromagnetic problems are generally classified into two main types: the emission and the excitation problems [6]. The calculation of the near-field enhancement factor for a given nanostructures is one of the example of the later case, which follows when a nanoparticle interacts with incident electromagnetic fields. The field that is generated by nanoparticle generally can be obtained by solving the Maxwell equations. Here we assume that the domain of calculation consists of non-magnetic, isotropic, and homogenous media with the relative permittivity $\epsilon_m(\mathbf{r},\omega)$. For time-harmonic electromagnetic fields $\mathbf{E}(\mathbf{r},t) = \mathbf{E}(\mathbf{r})e^{-i\omega t}$ and $\mathbf{B}(\mathbf{r},t) = \mathbf{B}(\mathbf{r})e^{-i\omega t}$, we have

$$\nabla \cdot \mathbf{H} = 0, \tag{2.24}$$

$$\nabla \cdot \mathbf{D} = 0, \tag{2.25}$$

$$\nabla \times \mathbf{E} = i\omega\mathbf{B}, \tag{2.26}$$

$$\nabla \times \mathbf{B} = \mu_0\mathbf{J} - i\omega\mu_0\epsilon_0\epsilon_m\mathbf{E}. \tag{2.27}$$

Apart from the Maxwell Equations (2.24)-(2.27), the following boundary conditions is applied at the interface of medium 1 and medium 2 by assuming no surface magnetic

field or charge:

$$\hat{\mathbf{n}} \times (\mathbf{E}_1 - \mathbf{E}_2) = 0; \tag{2.28}$$

$$\hat{\mathbf{n}} \cdot (\mathbf{D}_1 - \mathbf{D}_2) = 0, \tag{2.29}$$

where $\hat{\mathbf{n}}$ is the unit vector normal to the interface. For an arbitrary vector $\mathbf{F}$, we apply the identity $\nabla \times (\nabla \times \mathbf{F}) = \nabla(\nabla \cdot \mathbf{F}) - \nabla^2\mathbf{F}$ on both Eqs. (2.26) and (2.27). By substituting $\mathbf{J}$ as a linear function of $\mathbf{E}$ as given by Eq. (2.12), hence

$$-\nabla^2\mathbf{E} = \frac{\omega^2}{c^2}\left(\epsilon_m + \frac{i\sigma}{\epsilon_0\omega}\right)\mathbf{E}; \tag{2.30}$$

$$-\nabla^2\mathbf{B} = \frac{\omega^2}{c^2}\left(\epsilon_m + \frac{i\sigma}{\epsilon_0\omega}\right)\mathbf{B}, \tag{2.31}$$

The expression $\epsilon_m + \frac{i\sigma}{\epsilon_0\omega}$ is none other than the optical conductivity provided by Eq. (2.14). By defining the complex wave vector $\tilde{k} = \frac{\omega}{c}\sqrt{\epsilon_m}$, Eqs. (2.30) and (2.31) can be written in more simplified forms as

$$\nabla^2\mathbf{E} + \tilde{k}^2\mathbf{E} = 0, \tag{2.32}$$

$$\nabla^2\mathbf{B} + \tilde{k}^2\mathbf{B} = 0. \tag{2.33}$$

The Eqs. (2.32) and (2.33) are known as the Helmholtz Equations. The analytical solutions of the Helmholtz Equations describing the scattering of electromagnetic waves by homogenous sphere and cylinder which take forms the infinite series of vector spherical harmonics (VSH) [6], are provided by formalism of the Mie thory. In the context of near-field spectroscopy, the Mie theory is used to describe the plasmonic properties of individual nanoparticle whose size is less or equal to the wavelength of light, which is commonly approximated as a sphere [21, 6], and therefore for nano-structures with non-spherical shapes, its utility is rather limited. Thorough discussions on mathematical details of the Mie theory are contained in some works, e.g. references [6, 14].

In this work, the calculation of the near-field enhancement is performed within the framework the quasi-static approximation (QSA). In the QSA the propagation of the electromagnetic fields around the material are treated to be instaneous, which is satisfied by letting the speed of light in the Maxwell equations towards infinity ($c \to \infty$), and thus the retardation effects of the fields are neglected [6, 57]. In other words, the external electric field from the electromagnetic wave is regarded as spatially

static field with time-harmonic dependence, and the frequency effect of electromagnetic wave on the material is incorporated in its complex optical relative permittivity [6]. The mathematical formulation describing the excitation problems given by Eqs. (2.24)-(2.29) reduce into a simpler form as follows [6]:

$$\begin{aligned} \nabla \times \mathbf{E} &= 0, \\ \nabla \cdot \mathbf{D} &= 0, \\ \mathbf{n} \times (\mathbf{E}_1 - \mathbf{E}_2) &= 0, \\ \mathbf{n} \cdot (\mathbf{D}_1 - \mathbf{D}_2) &= 0. \end{aligned} \tag{2.34}$$

The consequence of this approximation is that the calculation of electric field can be performed by solving the Laplace equation instead of the full electromagnetic problems. Because of the scalar properties of the Laplace Equation, the solutions of the QSA are much easier to acquire, and therefore QSA is useful to describe the interaction of electromagnetic waves with a body whose spatial dimension is significantly smaller than the wavelength of the light λ, such as the near-field excitation in the nanoparticle or nanostructure (in the order of few-tens nm) as a response of the irradiation by visible light ($\lambda \approx 390-700$ nm), which is justified since the propagation of electric of the light around the nano-materials can be regarded as instaneous which in return generates negligible retardation effects. In the following sub-section, we apply QSA formulation given by Eq. (2.34) in the case of a small spherical particle exposed external electric field from an electromagnetic wave.

2.2.1 Near-Field Enhancement around Spherical Nanoparticle

In order to illustrate the properties of near-field excitation in a particular case, here we provide a classical example of a calculation using QSA, which can be found in some textbooks discussing plasmonics or nano-optics, e.g. [16, 19, 22]. The scheme of the problem is given by Fig. 2.3, which shows the illumination of homogenous sphere with radius a and complex permittivity $\epsilon_s(\omega)\epsilon_0$ by the external electric field from light at frequency ω. Here we assume that the radius the sphere is much smaller than the wavelength of light ($a \ll \lambda$), thus the electric field can be written as a spatially constant field $\mathbf{E} = E_0\hat{\mathbf{z}}$. The particle is surrounded by isotropic and non-absorbing

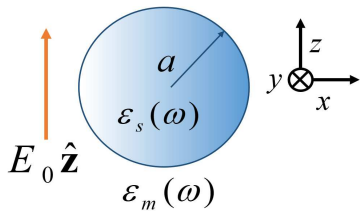

Figure 2.3 Homogenous sphere in the static electric field E_0.

medium with dielectric constant $\epsilon_m(\omega)\epsilon_0$. In order to obtain the electric field, firstly we solve the Laplace equation for electrostatic potential V. The Laplace Equation in the spherical coordinate is written as

$$\frac{1}{r^2}\frac{\partial}{\partial r}\left(r^2\frac{\partial V}{\partial r}\right)+\frac{1}{r^2\sin\theta}\frac{\partial}{\partial\theta}\left(\sin\theta\frac{\partial V}{\partial\theta}\right)+\frac{1}{r^2\sin^2\theta}\frac{\partial^2 V}{\partial\phi^2}=0. \tag{2.35}$$

We employ the separation of variables method by writing the scalar electric potential as $V(r,\theta,\phi)=R(r)Y(\theta,\phi)$, the Eq. (2.35) becomes

$$\left[\frac{1}{R(r)}\frac{\partial}{\partial r}\left(r^2\frac{\partial R(r)}{\partial r}\right)\right]+\left[\frac{1}{Y(\theta,\phi)\sin\theta}\frac{\partial}{\partial\theta}\left(\sin\theta\frac{\partial Y(\theta,\phi)}{\partial\theta}\right)+\frac{1}{Y(\theta,\phi)\sin^2\theta}\frac{\partial^2 Y(\theta,\phi)}{\partial\phi^2}\right]=0. \tag{2.36}$$

Further steps of the solution requires writing the first and second terms in the left-hand side of Eq. (2.36) as constants. As we know a general solution of the Laplace Equation, we equate the first(second) terms in the left-hand side of Eq. (2.36) with $\pm l(l+1)$, therefore

$$r^2\frac{\partial^2 R(r)}{\partial r^2}+2r\frac{\partial R(r)}{\partial r}-l(l+1)R(r)=0; \tag{2.37}$$

$$\sin\theta\frac{\partial}{\partial\theta}\left(\sin\theta\frac{\partial Y(\theta,\phi)}{\partial\theta}\right)+\frac{\partial^2 Y(\theta,\phi)}{\partial\phi^2}+l(l+1)\sin^2\theta Y(\theta,\phi)=0. \tag{2.38}$$

By separating the azimuthal part in the Eq. (2.38) as $Y(\theta,\phi)=\Theta(\theta)\Phi(\phi)$ and writing

$$\frac{\sin\theta}{\Theta(\theta)}\frac{\partial}{\partial\theta}\left(\sin\theta\frac{\partial\Theta(\theta)}{\theta}\right)+l(l+1)\sin^2\theta=m^2, \tag{2.39}$$

therefore

$$\frac{1}{\sin\theta}\frac{\partial}{\partial\theta}\left(\sin\theta\frac{\partial\Theta(\theta)}{\partial\theta}\right)+\left(l(l+1)-\frac{m^2}{\sin^2\theta}\right)\Theta(\theta)=0, \tag{2.40}$$

$$\frac{\partial^2\Phi(\phi)}{\partial\phi^2}+m^2\Phi(\phi)=0. \tag{2.41}$$

The solution of Eq. (2.40) is generally known as the associated Legendre polynomials $P_l^m(\cos\theta)$, while it can be seen that for any constant A, the function $\Phi(\phi)=Ae^{im\phi}$ satisfies the Equation (2.41). However, since the electric field is polarized along z-direction $\mathbf{E}_0 = E_0\hat{\mathbf{z}} = E_0(\cos\theta\hat{\mathbf{r}} - \sin\theta\hat{\boldsymbol{\theta}})$, the azimuthal symmetry applies which means that the solution for $Y(\theta,\phi)$ does not depend on ϕ. This condition implies $m=0$, and therefore the solution for azimuthal part is given by

$$Y(\theta,\phi)=P_l(\cos\theta), \tag{2.42}$$

where $P_l(\cos\theta)$ is the Legendre polynomials of order-l. The radial part $R(r)$ can be solved by expressing the function as the power series in the form

$$R(r)=\sum_{l=0}^{\infty}B_n r^n. \tag{2.43}$$

Inserting Eq. (2.43) into Eq. (2.37) yields

$$\sum_{l=0}^{\infty}B_n r^n[n(n+1)-l(l+1)]=0, \tag{2.44}$$

which gives $n=l,-l-1$. The general solution of Eq. (2.35) is given by

$$V(r,\theta)=\sum_{l=0}^{\infty}\left[C_l r^l+\frac{D_l}{r^{l+1}}\right]P_l(\cos\theta), \tag{2.45}$$

where C_l and D_l are arbitrary constants to be determined by the boundary conditions. Now we apply the proper boundary conditions to obtain excact form of the potentials inside and outside the sphere, V_{in} and V_{out} respectively. Inside the sphere ($r<a$) the term of $\frac{D_l}{r^{l+1}}$ diverges as $r\to 0$, thus in this region $D_l=0$ for all l, that is

$$V_{\text{in}}=\sum_{l=0}^{\infty}C_l r^l P_l(\cos\theta). \tag{2.46}$$

Here we only consider solution for lowest-order mode which can be obtained by only including $l=1$ in the derivation. Outside the sphere ($r>a$), the incoming field

$E_0 \cos\theta$ must be recovered at large r, which means that $V_{\text{out}} = -E_0 r \cos\theta$ as $r \to \infty$. This requirement demands that $C_1 = -E_0$. The value of D_1 shall be determined later. Since $P_1(\cos\theta) = \cos\theta$, thus

$$V_{\text{out}} = \left[-E_0 r + \frac{D_1}{r^2} \right] \cos\theta. \tag{2.47}$$

The lowest-mode solution is finally obtained by applying boundary conditions for electric and displacement fields, $\mathbf{E}$ and $\mathbf{D}$ respectively, as stated in Eqs. (2.28) and (2.29). The corresponding boundary conditions in spherical coordinate are respectively expressed as

$$\left(\frac{\partial V_{\text{in}}}{\partial \theta} \right)_{r=a} = \left(\frac{\partial V_{\text{out}}}{\partial \theta} \right)_{r=a}, \tag{2.48}$$

$$\epsilon_s \left(\frac{\partial V_{\text{in}}}{\partial r} \right)_{r=a} = \epsilon_m \left(\frac{\partial V_{\text{out}}}{\partial r} \right)_{r=a}. \tag{2.49}$$

Therefore the potentials inside and outside the sphere are given by

$$V_{\text{in}}(\mathbf{r}) = -\frac{3\epsilon_m}{\epsilon_s + 2\epsilon_m} E_0 r \cos\theta, \tag{2.50}$$

$$V_{\text{out}}(\mathbf{r}) = -E_0 r \cos\theta + \frac{\epsilon_s - \epsilon_m}{\epsilon_s + 2\epsilon_m} E_0 r \cos\theta \frac{a^3}{r^2}. \tag{2.51}$$

The electric fields inside and outside the sphere are immediately obtained by taking the gradient of the corresponding potentials $\mathbf{E}_{\text{in,out}} = -\nabla V_{\text{in,out}}$. Introducing the variables of dipole moment $\mathbf{p}$ and polarizability α defined as

$$\mathbf{p} \equiv 4\pi\epsilon_m\epsilon_0\alpha\mathbf{E}_0, \tag{2.52}$$

$$\alpha \equiv a^3 \frac{\epsilon_s - \epsilon_m}{\epsilon_s + 2\epsilon_m}, \tag{2.53}$$

the electric fields are then given by

$$\mathbf{E}_{\text{in}}(\mathbf{r}) = \frac{3\epsilon_m}{\epsilon_s + \epsilon_m} \mathbf{E}_0, \tag{2.54}$$

$$\mathbf{E}_{\text{out}}(\mathbf{r}) = \mathbf{E}_0 + \frac{1}{4\pi\epsilon_m\epsilon_0 r^3} [3\hat{\mathbf{r}}(\hat{\mathbf{r}} \cdot \mathbf{p}) - \mathbf{p}]. \tag{2.55}$$

Finally, the time-dependent electric fields are expressed as

$$\mathbf{E}_{\text{in,out}}(\mathbf{r}, t) = \mathbf{E}_{\text{in,out}}(\mathbf{r}) e^{-i\omega t}. \tag{2.56}$$

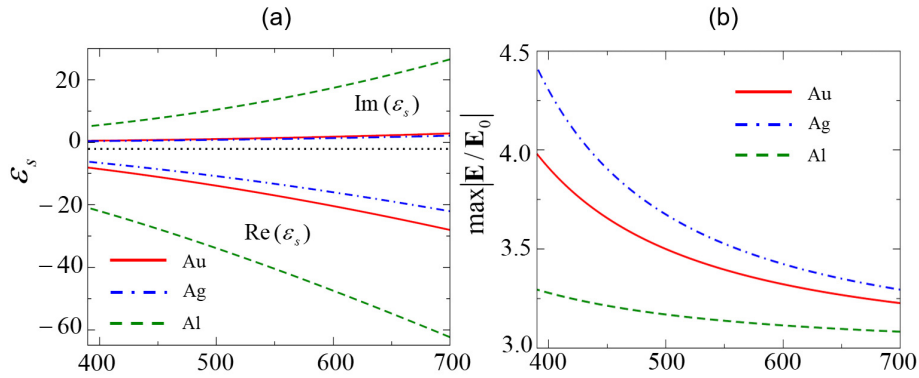

Figure 2.4 (a) Optical relative permittivity ϵ_s of Au, Ag, and Al spheres of radius 10 nm. The Drude fitting parameters are taken from reference [56]. The dotted black line represents the value Re(ϵ_s)=-2. (b) The maximum near-field enhancement of materials in (a), calculated by using Eq. 2.55.

The second term in the right-hand side of Eq. (2.55) is exactly the expression of near-field of oscillating dipole from the Eq. (1.6), and for this reason the lowest mode of excitation ($l = 1$) is called dipole excitation [21]. It is also shows that the near-field enhancement at a given wavelength which can be defined as $\frac{\mathbf{E}}{\mathbf{E}_0(\lambda)}$ (maximum at $r = a$ and $\cos\theta = 0$) is only determined by the relative permittivities of sphere and the surrounding medium. Fig. 2.4 compares the wavelength-dependence of Au, Ag, and Al nano-spheres optical relative permittivities (a=10 nm) at the visible region (λ=390-700 nm) and the maximum near-field enhancement around the nanoparticle placed in vacuum. An example of the near-field distribution normalized to the incoming field is depicted by Fig. 2.5. From the Fig. 2.4, it is observed that maximum near-field enhancements in the vicinity of Au and Ag spherical nanoparticles are siginificantly higher compared to the Al counterpart, because the real and imaginary parts of their relative permittivities are close to the values leading the dipole resonance, in which the near-field enahancement factor tends to be very large. Theoretically, in non-arbsorbing medium the dipole resonance occurs when following condition is fulfilled:

$$\mathrm{Re}(\epsilon_s) = -2\epsilon_m, \ \mathrm{Im}(\epsilon_s) = 0, \tag{2.57}$$

also knowsn as Fröhlich condition [16].

The inclusion of $l > 1$ in the solution of the Laplace Equation leads to the occurence of multipolar excitations. For example, when $l = 2$ both dipole and quadrupole modes

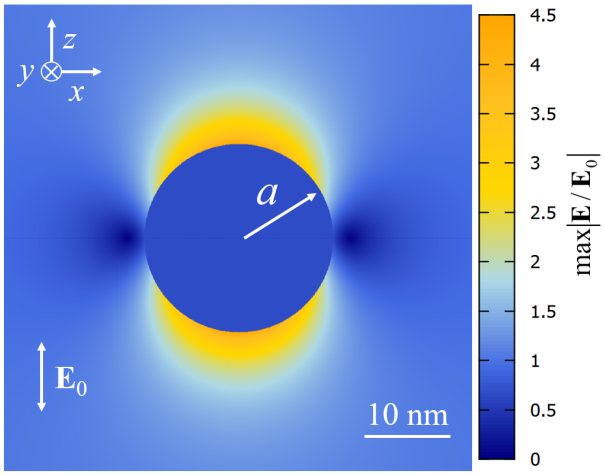

Figure 2.5 Near-field enhancement around Ag spherical nanoparticle (a=10 nm) at excitation wavelength λ=400 nm.

contribute to the excitation condition [21]. However, for many purposes, the lowest-mode excitation is adequate to describe the optical properties of small nanoparticles illuminated by visible or near-infrared radiation [16], since if the size of the corresponding nanoparticles are considerably small to the wavelength of the illuminating light, the contributions of higher order excitations are negligibly small compared to the dipole excitation [21]. The problems on the limit of QSA approximation related to the size of nanostructures shall be addreessed in the last Sub-section of QSA.

2.2.2 Quasi-static Finite-Difference Method

The simplest model of describing near-field enhancement around the tip is the quasi-static sphere as previously described [20]. To obtain the behavior of near-field as well as its resonant condition for more realistic shape of the tips, the Laplace Equation have been solved analytically for some generalized geometry, e.g. spheroids [58, 59, 6] and paraboloid [60]. For more complicated shapes, the analytical solution is practically difficult or otherwise impossible to obtain. To overcome this limitation, some methods have been devised to perform the calculations numerically, such as boundary element method (BEM) [60] and discrete-dipole approximation (DDA) [59, 21]. One of the well-known numerical method to solve various electromagnetics problems within the

quasi-static approximation is finite-difference method (FDM) [61, 20], which basically expands the derivatives of a given function or variable into a finite-difference scheme by discretization of calculation domain into set of lattices called mesh. Thus, the differential equation can be solved by numerical approximation. In the FDM for solving quasi-static problems, the square mesh is commonly employed to discretize the spatial position. For example, the position of a point P from the origin in the two-dimensional domain is expressed as:

$$(x_i, y_j) = (ih, jh),\ i, j \in \mathbb{Z}, \tag{2.58}$$

with h is defined as a small distance between any two neighboring points. The spatial square mesh of the domain is illustrated in Fig. 2.6(a), in which the values of other variables relevant to the calculation are stored. In order to obtain a finite-difference scheme of the second-order derivative of scalar potential V given in the Laplace equation, we evaluate V at the distance h from the point P with Taylor's series as follows:

$$\begin{aligned} V(x_i \pm h, y_j) =& V(x_i, y_j) \pm \frac{\partial V(x_i, y_j)}{\partial x} h + \frac{\partial^2 V(x_i, y_j)}{\partial x^2} h^2 \\ &+ \frac{\partial^3 V(x_i, y_j)}{\partial x^3} h^3 + O(h^4), \end{aligned} \tag{2.59}$$

$$\begin{aligned} V(x_i, y_j \pm h) =& V(x_i, y_j) \pm \frac{\partial V(x_i, y_j)}{\partial y} h + \frac{\partial^2 V(x_i, y_j)}{\partial y^2} h^2 \\ &- \frac{\partial^3 V(x_i, y_j)}{\partial y^3} h^3 + O(h^4). \end{aligned} \tag{2.60}$$

Hereafter we denote $V(x_i, y_j)$ as $V_{i,j}$. By inserting Eqs. (2.59) and (2.60) into the Laplace equation

$$\nabla^2 V_{i,j} = \frac{\partial^2 V_{i,j}}{\partial x^2} + \frac{\partial^2 V_{i,j}}{\partial y^2} = 0, \tag{2.61}$$

therefore the potential $V_{i,j}$ can be solved directly, given by

$$V_{i,j} = \frac{V_{i+1,j} + V_{i-1,j} + V_{i,j+1} + V_{i,j-1}}{4} + O(h^4). \tag{2.62}$$

By neglecting fourth-order error $O(h^4)$, Eq. (2.62) shows that the value of $V_{i,j}$ is the average of its four nearest-neighbor lattices, as depicted by Fig. 2.6(b).

For inhomogenous domain consisting two or more media with different dielectric constants, the relative permittivity as the function of the position $\epsilon(\mathbf{r}, \omega)$ needs to be incorporated into the mesh. For a moment, we assume that the media are dielectrics,

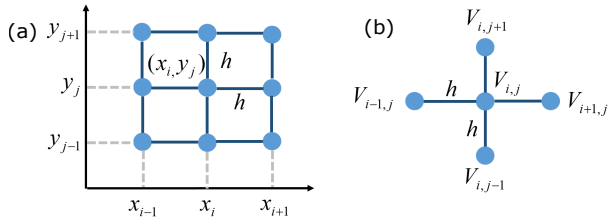

Figure 2.6 (a) Position and (b) potential mesh in finite-difference domain.

whose imaginary part of the relative permittivity is with zero or negligible. We begin with the Gauss law, written as

$$\nabla \cdot [\epsilon(\mathbf{r}, \omega) \nabla V(\mathbf{r})] = 0. \tag{2.63}$$

The Gauss Divergence Theorem for two-dimensional system is then applied into the Eq. (2.63). In two-dimensional system, it transforms the integration with respect to the differential surface area $\mathrm{d}S = \mathrm{d}x\mathrm{d}y$ into the contour integration in the form

$$\oint_{S_{i,j}} \nabla \cdot [\epsilon(\mathbf{r}, \omega) \nabla V(\mathbf{r})] \, \mathrm{d}S = \oint_{l_{i,j}} \epsilon(\mathbf{r}, \omega) \nabla V(\mathbf{r}) \cdot \hat{\mathbf{n}} \, \mathrm{d}l, \tag{2.64}$$

where $\hat{\mathbf{n}}$ is the unit vector normal to the path of integration l. The contour integral is performed along the interface separating media with dielectric constants ϵ_1 and ϵ_2, and is decomposed into the paths l_1, l_2, l_3, and l_4, as shown by Fig. 2.7(a). The finite-difference counterpart for the corresponding integration is given by Fig. 2.7(b), in which the relative permittivity of point (x_i, y_j) is denoted by $\epsilon_{i,j}$. By using trapezoidal rule, in which the continous integration of a a given function $f(x)$ from $x_{i-1} = x_i - h$ to $x_{i+1} = x_i + h$ with respect to $\mathrm{d}x$ can be numerically evaluated as [62]:

$$\int_{x_{i-1}}^{x_{i+1}} f(x)\mathrm{d}x = \frac{h}{2}[f(x_{i-1}) + 2f(x_i) + f(x_{i+1})] + O(h^3), \tag{2.65}$$

the integration along l_1 is therefore approximated as

$$\begin{aligned} \int_{l_1} \epsilon(\mathbf{r}, \omega) \frac{\partial V}{\partial x} \, \mathrm{d}y \approx & \frac{1}{2} \left(\frac{V_{i+2,j} - V_{i+1,j}}{h} + \frac{V_{i+1,j} - V_{i,j}}{h} \right) \times \\ & \left(\frac{\epsilon_{i+1,j+1} + 2\epsilon_{i+1,j} + \epsilon_{i+1,j-1}}{2} \right) 2h \\ = & (V_{i+2,j} - V_{i,j}) \frac{\epsilon_{i+1,j+1} + 2\epsilon_{i+1,j} + \epsilon_{i+1,j-1}}{2}, \end{aligned} \tag{2.66}$$

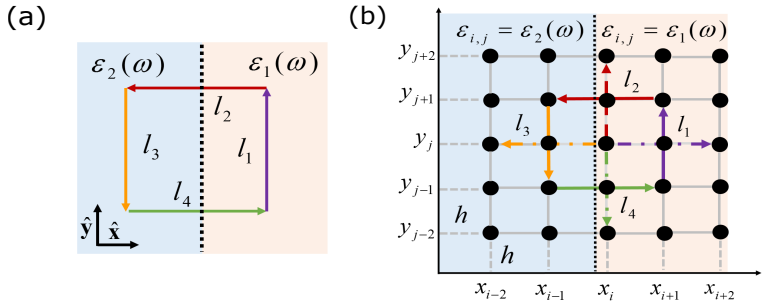

Figure 2.7 (a) Continous and (b) discrete contour integration paths in the right-hand side of Equation 2.64. The interface between media is depicted with dotted lines. Violet, red, orange, and green arrows represent paths l_1, l_2, l_2, and l_4, respectively. In (b), the electric field component normal to each path in the integration is depicted as the dashed arrow with the same color.

similarly, the integrations along l_2, l_3, and l_4 are given by

$$\int_{l_2} \epsilon(\mathbf{r},\omega)\frac{\partial V}{\partial y}\,\mathrm{d}x \approx (V_{i,j+2} - V_{i,j})\frac{\epsilon_{i+1,j+1} + 2\epsilon_{i,j+1} + \epsilon_{i-1,j+1}}{2}, \tag{2.67}$$

$$\int_{l_3} \epsilon(\mathbf{r},\omega)\frac{\partial V}{\partial x}\,\mathrm{d}y \approx (V_{i-2,j} - V_{i,j})\frac{\epsilon_{i-1,j+1} + 2\epsilon_{i-1,j} + \epsilon_{i-1,j-1}}{2}, \tag{2.68}$$

$$\int_{l_4} \epsilon(\mathbf{r},\omega)\frac{\partial V}{\partial y}\,\mathrm{d}x \approx (V_{i,j-2} - V_{i,j})\frac{\epsilon_{i+1,j-1} + 2\epsilon_{i,j-1} + \epsilon_{i-1,j-1}}{2}. \tag{2.69}$$

By combining the Eqs. (2.66)-(2.69), the potential $V_{i,j}$ can be solved as

$$V_{i,j} \approx \frac{V_{i+2,j}\beta_{i,j}^{(1)} + V_{i,j+2}\beta_{i,j}^{(2)} + V_{i-2,j}\beta_{i,j}^{(3)} + V_{i,j-2}\beta_{i,j}^{(4)}}{\beta_{i,j}^{(1)} + \beta_{i,j}^{(2)} + \beta_{i,j}^{(3)} + \beta_{i,j}^{(4)}}, \tag{2.70}$$

where the definitions of $\beta_{i,j}^{(n)}, n = 1-4$ are given as follows:

$$\begin{aligned} \beta_{i,j}^{(1)} &\equiv \frac{\epsilon_{i+1,j+1} + 2\epsilon_{i+1,j} + \epsilon_{i+1,j-1}}{2}, \quad \beta_{i,j}^{(2)} \equiv \frac{\epsilon_{i+1,j+1} + 2\epsilon_{i,j+1} + \epsilon_{i-1,j+1}}{2}, \\ \beta_{i,j}^{(3)} &\equiv \frac{\epsilon_{i-1,j+1} + 2\epsilon_{i-1,j} + \epsilon_{i-1,j-1}}{2}, \quad \beta_{i,j}^{(4)} \equiv \frac{\epsilon_{i+1,j-1} + 2\epsilon_{i,j-1} + \epsilon_{i-1,j-1}}{2}. \end{aligned} \tag{2.71}$$

Note that in the case of homogenous domain, $\beta_{i,j}^{(n)}$ is constant and therefore Eq. (2.70) is accordingly reduced to Eq. (2.62) as expected. The first step to calculate electric field distribution is by assigning an appropiate initial value for each $V_{i,j}$. In the iterative process that follows, the potential value at $(n+1)$-th iteration $V_{i,j}^{(n+1)}$ is then updated from the values of its four nearest-neighbor potentials obtained from the previous iteration, by utilizing finite-difference result derived in Eq. (2.70). This

updating algorithm is expressed as

$$V_{i,j}^{(n+1)} = \frac{V_{i+2,j}^{(n)}\beta_{i,j}^{(1)} + V_{i,j+2}^{(n)}\beta_{i,j}^{(2)} + V_{i-2,j}^{(n)}\beta_{i,j}^{(3)} + V_{i,j-2}^{(n)}\beta_{i,j}^{(4)}}{\beta_{i,j}^{(1)} + \beta_{i,j}^{(2)} + \beta_{i,j}^{(3)} + \beta_{i,j}^{(4)}}, \tag{2.72}$$

The iterative loop is then repeated until the difference between $V_{i,j}^{(n+1)}$ and $V_{i,j}^{(n)}$ falls in the range of some acceptable error value. When the criteria of convergence is achieved, the electric field of the corresponding point is then calculated by taking the gradient of the potential as follows:

$$\mathbf{E}_{i,j}^{(n+1)} = -\frac{V_{i+2,j}^{(n+1)} - V_{i,j}^{(n+1)}}{2h}\hat{\mathbf{x}} - \frac{V_{i,j+2}^{(n+1)} - V_{i,j}^{(n+1)}}{2h}\hat{\mathbf{y}} \tag{2.73}$$

The quasi-static finite-difference method formerly explained requires generalization for a domain consisting conductive materials where the induced current density is included in the calculation [61]. By using Eq. (2.12) for induced current $\mathbf{J}$ and then applying the identity $\nabla \cdot (\nabla \times \mathbf{F}) = 0$ on the Ampere law given in Eq. (2.27), therefore

$$\nabla \cdot \left[\left(\epsilon_m + \frac{i\sigma}{\epsilon_0 \omega} \right) \mathbf{E} \right] = 0. \tag{2.74}$$

In the harmonic time-varying system, the expression of the electromagnetic fields include vector potential $\mathbf{A}(\mathbf{r})$, and are given by

$$\mathbf{E}(\mathbf{r}) = -\nabla V(\mathbf{r}) + i\omega \mathbf{A}(\mathbf{r}); \tag{2.75}$$

$$\mathbf{B}(\mathbf{r}) = \nabla \times \mathbf{A}(\mathbf{r}). \tag{2.76}$$

Thus, in order to find $\mathbf{E}(\mathbf{r})$, both $V(\mathbf{r})$ and $\mathbf{A}(\mathbf{r})$ must be solved simultaneously in the first-hand. However, in the QSA the contribution of the vector potential to the electric-field is negligible at low frequency, i.e. $i\omega\mathbf{A}(\mathbf{r}) \approx 0$, this condition implies that $\mathbf{E}(\mathbf{r}) \approx -\nabla V(\mathbf{r})$. Therefore the Eq. (2.63) can be rewritten as

$$\nabla \cdot [(\epsilon_r^{(1)} + i\epsilon_r^{(2)}) \nabla V(\mathbf{r})] = 0. \tag{2.77}$$

We have shown that quasi-static finite-difference method is also applicable to calculate the electric field in the domain in which metallic material is present, simply by using complex relative permittivity instead of the real-valued one. With this method, it is possible to calculate the near-field distribution surrounding nanostructure for any

arbitrary shape. Indeed, this method is also applicable to simulate local electric field response of system consisting configuration of nano-materials, e.g. arrays of 2D nano-odisks embedded in a low dielectric medium [63, 64]. We shall use the previously explained procedure to calculate near-field enhancement of in the vicinity of Au tips placed in the vacuum, presented in the Chapter 3.

2.2.3 Validity and Limit of Quasi-Static Approximation

In this Sub-section, we address the limit the validity and limit of QSA which is related to the ratio between the spatial dimension of nanostructures and the wavelength of the illuminating electromagnetic wave, generally assumed as a plane wave. The common circumstance of the calculation with QSA consists of nanostructure and and non-absorbing medium. Supposing that the plane wave is propagating along x-direction in the Cartesian coordinate, the spatial dependence of the electric is described as:

$$E(x) = E_0 e^{i\widetilde{n}kx}, \tag{2.78}$$

where $\widetilde{n}$ is the complex refractive index of the medium or body in which the plane wave propagates. We denote D as the largest dimension of the body and λ as the wavelength of electromagnetic wave. Since in QSA the radiating electric field is considered as spatially static, therefore following condition must be satisfied for both inside and and ouside the body [6]:

$$|\widetilde{n}kD| \ll 1, \text{ or } \frac{D}{\lambda} \ll \left|\frac{1}{2\pi\widetilde{n}}\right|. \tag{2.79}$$

Based on this imposed condition, the typical limit of which QSA can be regarded as valid is $D \approx \frac{\lambda}{20}$ or possibly $D \approx \frac{\lambda}{10}$ [6]. This result is confirmed by the work of McLeod et al. [65] who compares the calculations of near-field enhancements around ellipsoid and hyperboloid tips with the quasi-static and electrodynamics finite-element method (FEM). Length and radius of the tips (placed above SiO_2/Si layers plane) are L and a, respectively. The result is summarized in Fig. 2.8, which shows that the quasi-static approximation predicts monotonic growth of near-field enhancement as L increases while a is kept constant. This behavior is attributed to the lightning-rod effect which depends of the geometric 'sharpness' of the tips, quantitatively parameterized by $\frac{L}{a}$ [65]. The quasi-static results depart from the more realistic electrodynamics

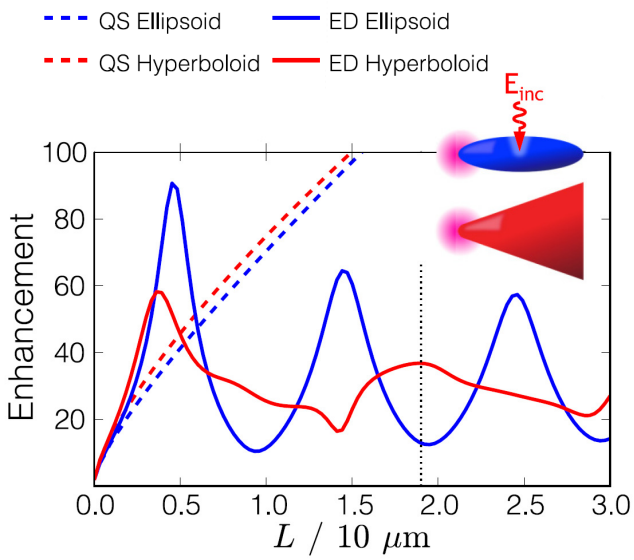

Figure 2.8 Calculation of near-field enhancement around ellipsoid and parabolic tips with quasi-static (QS) and electrodynamic (ED) FEM. The illuminating electric field E_{inc} is perpendicular to the tip's axes [65].

calculations near the probe length $L \approx \frac{\lambda}{10}$. For the visible wavelength, this means that the largest dimension of the body considerably valid in the quasi-static system is in the range of 39-70 nm. However, in general cases the limit of QSA is difficult to determine precisely [6]. Another criteria for this limit is given by Demming et al [60], who state that QSA is valid as long as the largest dimension of the body is smaller than Rayleigh length R, defined as $R = \frac{\lambda}{2\pi}$. Some authors even consider that for the optical wavelength, QSA is adequate to describe the optical properties of a body whose size is below 100 nm [66, 16].

2.3 Electron-Light Interactions in Graphene

2.3.1 Electron-Photon Hamiltonian

By using the near-field obtained the previous Sub-section, let us describe the interaction of electron with an external electromagnetic field by considering the Hamiltonian of electron in the corresponding condition. The momentum of electron $\mathbf{p}$ is substituted by canonical momentum in the form $\mathbf{p} - e\mathbf{A}(\mathbf{r})$, where e is the elementary charge and

$\mathbf{A}$ is the potential vector. The total Hamiltonian is generally given by

$$\mathcal{H}(\mathbf{r},t) = \frac{[\mathbf{p} - e\mathbf{A}(\mathbf{r},t)]^2}{2m} + U(\mathbf{r}), \tag{2.80}$$

in which m and $U(\mathbf{r})$ are the electronic mass and potential energy of a given system, respectively. By transforming the momentum $\mathbf{p}$ into the respective operator form $\mathbf{p} \to \frac{\hbar}{i}\nabla$, and adapting the Coulomb gauge $\nabla \cdot \mathbf{A} = 0$, Eq. (2.80) becomes

$$\mathcal{H} \approx \left[\frac{p^2}{2m} + U(\mathbf{r})\right] + \left[-\frac{e\mathbf{A}\cdot\nabla}{m}\right] \equiv \mathcal{H}_0 + \mathcal{H}', \tag{2.81}$$

where $\mathcal{H}_0$ and $\mathcal{H}'$ correspondingly denote unperturbed and time-dependent perturbed Hamiltonians. In Eq. (2.81) we do not include the term $\propto A^2$ since in the visible light its value is very small compared with the term consisting linear-dependence of $\mathbf{A}$. Now we consider the relation between the vector potential $\mathbf{A}$ with the electric field $\mathbf{E}$. In the far-field case, there is no contribution of scalar potential $V(\mathbf{r})$ to the electric field, and therefore the relation can be directly established in the Eq. (2.75) by taking $V(\mathbf{r})$=0, hence

$$\mathbf{A} = \frac{\mathbf{E}}{i\omega}. \tag{2.82}$$

On the other hand, in near-field case described by the quasi-static approximation, we have to consider a different approach. By utilizing the Ampere law for vacuum ($\epsilon_r = 1$, $\mathbf{J} = 0$) as well as Eqs. (2.75) and (2.75), we have

$$\nabla \times \nabla \times \mathbf{A} = \frac{-1}{c^2}\left[\frac{\partial \nabla V}{\partial t} + \frac{\partial^2 \mathbf{A}}{\partial t^2}\right]. \tag{2.83}$$

By employing Coulomb gauge and assuming that $\mathbf{A}$ is a plane wave, i.e. $\mathbf{A}(\mathbf{r},t) = \mathbf{A}_0 e^{i(\mathbf{k}\cdot\mathbf{r}-\omega t)}$, then $\nabla\times\mathbf{A} = i\mathbf{k}\times\mathbf{A}$. In the quasi-static case, the second-order derivative term in the Eq. (2.83) can be excluded because the retarded time is omitted [57], therefore

$$\omega^2\mathbf{A} = \frac{\partial \nabla V}{\partial t}. \tag{2.84}$$

By substituting the right-hand side of Eq. (2.84) with $-i\omega[-\nabla V(\mathbf{r})] = -i\omega\mathbf{E}_{\mathrm{st}}(\mathbf{r})$, where $\mathbf{E}_{\mathrm{st}}(\mathbf{r})$ is the static electric field, thus again Eq. (2.82) prevails. In general, the perturbed electron-photon Hamiltonian is given by

$$\mathcal{H}' = \frac{e\hbar}{m\omega}\mathbf{E}\cdot\nabla, \tag{2.85}$$

in which **E** can be either electric far- or near-fields. In the next-Sub-section, we shall use the tight-binding graphene wave function to calculate the electron-photon matrix element.

2.3.2 Tight-binding Electron-Photon Matrix Element

The electron-photon matrix element describe the interaction between an electron in material with the external electric field from an incident light. Let us consider an electron at initial electronic state i, in which we denote $\mathbf{k}_i$ as electron wave vector. The electric field incites the electron to the finial state f and now its wave vector is denoted as $\mathbf{k}_f$. This process of electron excitation is accounted by the electron-photon matrix element, mathematically stated as

$$\begin{aligned} M_{\mathrm{e-opt}}(\mathbf{k},\mathbf{r}) &= \langle \Psi^f(\mathbf{k}_f,\mathbf{r})|\mathcal{H}'|\Psi^i(\mathbf{k}_i),\mathbf{r}\rangle \\ &= \frac{e\hbar}{m\omega}\langle \Psi^f(\mathbf{k}_f,\mathbf{r})|\mathbf{E}(\mathbf{r})\cdot\nabla|\Psi^i(\mathbf{k}_i,\mathbf{r})\rangle, \end{aligned} \tag{2.86}$$

where $\Psi^{i(f)}(\mathbf{k}_{i(f)})$ is the electron wave function at initial (final) electronic state. In the tight-binding method, the wave function of a system is expressed as the linear summation of its atomic orbitals (for this reason tight-binding method is also known as linear combination of atomic orbitals, LCAO). In the case of graphene, the 2s, $2p_x$, and $2p_y$ orbitals form the σ bonding which is responsible for the structural robustness of all carbon allotropes, while $2p_z$ orbital give rises to the π bonding whose energy is close to the Fermi level and largely determine of the optical properties of graphene in the visible region [31, 67]. Therefore, in this thesis, only the electron in $2p_z$ orbital is considered. Since there are two carbon atoms A and B, the wave function consists of **Bloch wave function**, $\phi_s^b(\mathbf{k})$ as well as its tight-binding coefficient $C_u^b(\mathbf{k})$, given by

$$\Psi^f(\mathbf{k},\mathbf{r}) = \sum_{u=\mathrm{A,B}} C_u^{\mathrm{b}}(\mathbf{k})\phi_u(\mathbf{k},\mathbf{r}),\ (\mathrm{b}=\mathrm{v,c}), \tag{2.87}$$

where indices v and c specify for valence and conduction bands, respectively. In graphene containing N carbon atoms, the Bloch wave function described as follows:

$$\phi_u(\mathbf{k},\mathbf{r}) = \frac{1}{\sqrt{N}}\sum_{j=1}^{N} e^{i\mathbf{R}_j^u}\varphi(\mathbf{r}-\mathbf{R}_j^u), \tag{2.88}$$

in which $\varphi(\mathbf{r}-\mathbf{R}_j^u)$ is the electron of $2p_z$ orbital at distance $\mathbf{R}_j^u$ from the origin. We need to define some variables before explicitly state the formulae for the tight-

binding coefficients. Referring to Fig. 1.6(b), we define $\boldsymbol{\delta}_n^{\mathrm{B}} \equiv \boldsymbol{\delta}_n$, $n = 1, 2, 3$, as the vectors connecting atom in B-sublattice to its three nearest-neighbor atoms in A sub-lattice. Conversely, we write $\boldsymbol{\delta}_n^{\mathrm{A}} = -\boldsymbol{\delta}_n^{\mathrm{B}}$ as the vectors from an A atom to its three nearest-neighbor B atoms. By using this information, the variables $f(\mathbf{k})$, its complex conjugate $f^*(\mathbf{k})$, and its absolute value $\omega(\mathbf{k})$ which are often employed in the tight-binding calculations of graphene can be calculated as

$$f(\mathbf{k}) \equiv \sum_{n=1}^{3} e^{i\mathbf{k}\cdot\boldsymbol{\delta}_n^{\mathrm{A}}} = e^{i\frac{k_x a}{\sqrt{3}}} + 2e^{-i\frac{k_x a}{2\sqrt{3}}}\cos(k_y a/2), \tag{2.89}$$

$$f^*(\mathbf{k}) \equiv \sum_{n=1}^{3} e^{i\mathbf{k}\cdot\boldsymbol{\delta}_n^{\mathrm{B}}} = e^{-i\frac{k_x a}{\sqrt{3}}} + 2e^{i\frac{k_x a}{2\sqrt{3}}}\cos(k_y a/2), \tag{2.90}$$

$$\omega(\mathbf{k}) \equiv \sqrt{f(\mathbf{k})f^*(\mathbf{k})} = \left[1 + 4\cos\left(\frac{k_y a}{2}\right)\cos\left(\frac{\sqrt{3}k_x a}{2}\right) + \cos^2\left(\frac{k_y a}{2}\right)\right]^{\frac{1}{2}}. \tag{2.91}$$

The explicit formulae of tight-binding coefficients are given by [67]:

$$\begin{aligned} C_{\mathrm{A}}^{\mathrm{v}}(\mathbf{k}) &= \frac{1}{\sqrt{2[1+s\omega(\mathbf{k})]}}\sqrt{\frac{f(\mathbf{k})}{\omega(\mathbf{k})}},\ C_{\mathrm{A}}^{\mathrm{c}}(\mathbf{k}) = \frac{1}{\sqrt{2[1-s\omega(\mathbf{k})]}}\sqrt{\frac{f(\mathbf{k})}{\omega(\mathbf{k})}}, \\ C_{\mathrm{B}}^{\mathrm{v}}(\mathbf{k}) &= \frac{1}{\sqrt{2[1+s\omega(\mathbf{k})]}}\sqrt{\frac{f^*(\mathbf{k})}{\omega(\mathbf{k})}},\ C_{\mathrm{B}}^{\mathrm{c}}(\mathbf{k}) = \frac{-1}{\sqrt{2[1-s\omega(\mathbf{k})]}}\sqrt{\frac{f^*(\mathbf{k})}{\omega(\mathbf{k})}}, \end{aligned} \tag{2.92}$$

where s is the overlap integral between atom A and B, defined by

$$s \equiv \langle\varphi(\mathbf{r} - \mathbf{R}_j^u - \boldsymbol{\delta}_n^{\mathrm{u}})|\varphi(\mathbf{r} - \mathbf{R}_j^u)\rangle. \tag{2.93}$$

In this thesis, we utilize s=0.129 [67]. By referring to Eq. (2.92), we derive some relations of tight-binding coefficients which is useful for later calculations as follows:

$$C_{\mathrm{A}}^{\mathrm{c}*}(\mathbf{k})C_{\mathrm{B}}^{\mathrm{v}}(\mathbf{k}) = -\left[C_{\mathrm{B}}^{\mathrm{c}*}(\mathbf{k})C_{\mathrm{A}}^{\mathrm{v}}(\mathbf{k})\right]^*, \tag{2.94}$$

$$C_{\mathrm{A}}^{\mathrm{c}*}(\mathbf{k})C_{\mathrm{A}}^{\mathrm{v}}(\mathbf{k}) = -\,C_{\mathrm{B}}^{\mathrm{c}*}(\mathbf{k})C_{\mathrm{B}}^{\mathrm{v}}(\mathbf{k}). \tag{2.95}$$

The wave function of graphene $2\mathrm{p_z}$ orbital is an odd function with respect to the z coordinate [67], and it is helpful to express the wave function in the terms of some well-known functions to obtain deeper understanding of its properties. In order to make possible the calculations of some fundamental variables analytically, the normalized wave function of graphene $2\mathrm{p_z}$ orbital has been fitted into Gaussian basis set in the form of [67]:

$$\varphi(\mathbf{r} - \mathbf{r}_0) = (z - z_0)\sum_{k=1}^{4} I_k \exp\left[\frac{-(\mathbf{r} - \mathbf{r}_0)^2}{2\sigma_k^2}\right]. \tag{2.96}$$

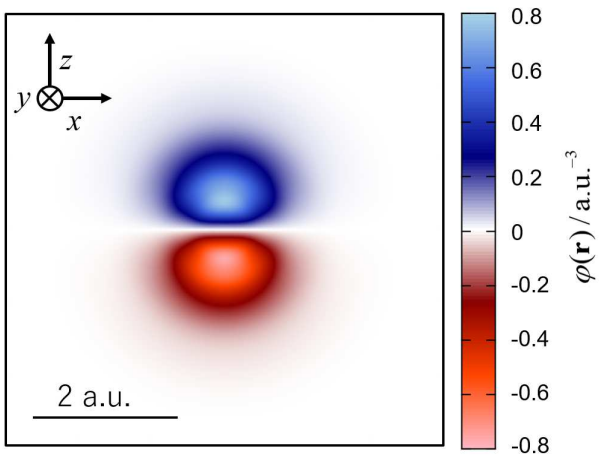

Figure 2.9 Wave function of graphene $2p_z$ orbital.

The Gaussian parameters in the Eq. (2.96) to fit an ab-initio calculation are given by Tabel 2.1. By using these values, we visualize the graphene $2p_z$ orbital in the xz plane centered at the origin, i.e. at $y = 0$, $\mathbf{r}_0 = 0$, and $z_0 = 0$ as shown by the Fig. 2.9, from which it is inferred that the length of orbital is around 2 a.u. = 1.058 Å.

k	1	2	3	4
I_k (a.u$^{-5/2}$)	0.05	0.41	1.06	1.05
σ_k (a.u)	2.16	0.91	0.13	0.39

Table 2.1: The Gaussian fitting parameters for the radial part of the electronic graphene 2p wave function [67] in the xz plane at $y = 0$.

2.3.3 Optical Absorption in Graphene

By using the tight-binding description of graphene, now we are ready to calculate the optical absorption and emission in its interaction with light. In the case of electromagnetic wave in the far-field regime, the electric field polarized in the **P** direction is simply written as

$$\mathbf{E}(t) = Ee^{\pm i\omega t}\mathbf{P}, \tag{2.97}$$

where the +(-) sign in the Eq. (2.97) specifies the emission (absorption) of a photon with frequency ω. Based on this information as well as Eq. (2.86), the matrix element

describing the absorption or emission of light whose frequency ω_{L} is given by

$$M_{\mathrm{e-opt}}(\mathbf{k}_i, \mathbf{k}_f) = \frac{e\hbar}{m\omega} E e^{i(\omega_f - \omega_i \pm \omega_{\mathrm{L}})} \mathbf{P} \cdot \mathbf{D}^{fi}(\mathbf{k}_i, \mathbf{k}_f), \tag{2.98}$$

where $\mathbf{D}^{fi}(\mathbf{k}_i, \mathbf{k}_f)$ is called the **dipole vector** between initial and final electronic states and is defined by

$$\mathbf{D}^{fi}(\mathbf{k}_i, \mathbf{k}_f) \equiv \langle \Psi^f(\mathbf{k}_f, \mathbf{r}) | \nabla | \Psi^i(\mathbf{k}_i, \mathbf{r}) \rangle. \tag{2.99}$$

Note that in the Eq. (2.98) the electric far-field is taken out from the integration since its magnitude is constant along the graphene plane. Furthermore, by recalling Eqs. (2.87) and (2.88) as well as tight binding coefficients relations given by Eqs. (2.94) and (2.95), it can be shown that the more explicit form of dipole vector describing transition from valence to conduction band is given as follows:

$$\mathbf{D}^{\mathrm{cv}}(\mathbf{k}) = -\frac{2\sqrt{3}}{a} m_{\mathrm{opt}} \mathrm{Re}\left[C_{\mathrm{B}}^{\mathrm{c}*}(\mathbf{k}) C_{\mathrm{A}}^{\mathrm{v}}(\mathbf{k}) \sum_{n=1}^{3} \exp(-i\boldsymbol{\delta}_n^{\mathrm{A}} \cdot \mathbf{k}) \boldsymbol{\delta}_n^{\mathrm{A}} \right], \tag{2.100}$$

where the variable m_{opt} is called **optical matrix element**, because its provision of describing the optical properties of π electron in graphene [67]. The optical matrix element is defined as

$$m_{\mathrm{opt}} \equiv \left\langle \varphi(\mathbf{r} - \boldsymbol{\delta}_n^{\mathrm{B}}) \left| \frac{\partial}{\partial x} \right| \varphi(\mathbf{r}) \right\rangle. \tag{2.101}$$

By using the Gaussian basis set in Eq. (2.96) as well as Table 2.1, the optical matrix element expressed in Eq. (2.101) can be calculated analytically, from which its value is obtained to be $m_{\mathrm{opt}} = 0.21$ a.u.$^{-1}$ [67]. It is informative to mention that since the product of atomic wave function and its derivative quickly descrease as the distance between atoms is increasing, only the nearest-neighbour coupling is considered [67].

There are two points to be clarified in the steps of calculation leading to the Eq. (2.100) to get a better comprehension of the properties of optical absorption in graphene that soon will be discussed. *First*, it is mentioned but not explicitly shown in [67] that the direction of the dipole vector is the opposite of that three vectors connecting atom A to atom B or vice versa in the form of:

$$\langle \varphi(\mathbf{r} - \boldsymbol{\delta}_n^{\mathrm{A(B)}}) | \nabla | \varphi(\mathbf{r}) \rangle = -\left\langle \varphi(\mathbf{r} - \boldsymbol{\delta}_n^{\mathrm{B}}) \left| \frac{\partial}{\partial x} \right| \varphi(\mathbf{r}) \right\rangle \boldsymbol{\delta}_n^{\mathrm{A(B)}}, \tag{2.102}$$

based on the reasoning that the vectors point along the bond between two atoms A and B, and the gradient yields vector which points away from the origin, because the wave function possesses positive value that is descreasing when moving away from the origin, i.e. the center of one wave function [67]. Referring to Eq. (2.98), then this result implies that the light polarized in z direction will result the zero value of the matrix element and consequently, as shall be demonstrated later, there is no optical absorption for the light in the corresponding polarization. *Second*, In the Eq. (2.100), the summation over all atomic sites gives the selection rule $\mathbf{k}_i = \mathbf{k}_f = \mathbf{k}$ which means that in far-field case the optical transition always occurs vertically, i.e. without change of electron wave vector. In the relation to original results in this thesis, In Chapter 4 we shall perform rigorous step-by-step calculation of optical matrix element which eventually confirms the result in Eq. (2.102), as well as demonstrate that the vertical transition is only a special case of electronic optical transition based on the argument of Fourier transform. In our case, the localized near-field on graphene plane placed few nanometers below the tip apex depends on the spatial position $\mathbf{R} = (x, y)$ is given by

$$\mathbf{E}(\mathbf{R}) = E_0 \sum_{\sigma=x,y,z} \boldsymbol{\eta}_\sigma(\mathbf{R}), \tag{2.103}$$

in which the near-field enhancement factor $\boldsymbol{\eta}_\sigma(\mathbf{R}) \equiv \frac{\mathbf{E}_\sigma(\mathbf{R})}{\mathbf{E}_0}$ is expressed as the summation of the Gaussian-based functions in order in order to enable the analytical calculations of relevant variables.

Finally, by using the Fermi golden rule, the transition probability or rate of graphene electron between initial and final states (valence and conduction bands, respectively) $W_{\mathrm{v}\to\mathrm{c}}$, due to the absorption of photon with energy ϵ_{L} is proportional to the square of optical matrix element in Eq. (2.98) given as follows:

$$W_{\mathrm{v}\to\mathrm{c}} \propto |\mathbf{P} \cdot \mathbf{D}^{\mathrm{cv}}(\mathbf{k})|^2 \delta(\epsilon_{\mathrm{c}}(\mathbf{k}_{\mathrm{c}}) - \epsilon_{\mathrm{v}}(\mathbf{k}_{\mathrm{v}}) - \epsilon_{\mathrm{L}}), \tag{2.104}$$

where δ is the Dirac delta function. From the Eq. (2.104), it can be shown that the optical absorption in the case of far-field is mainly determined by the polarization of light $\mathbf{P}$, which results the nodes observed around K and K' points in the Brillouin zone of graphene [67, 68]. We reproduce the calculations of transition probability for two different light polarizations $\mathbf{P} = (P_x, P_y)$, depicted by Fig. 2.10.

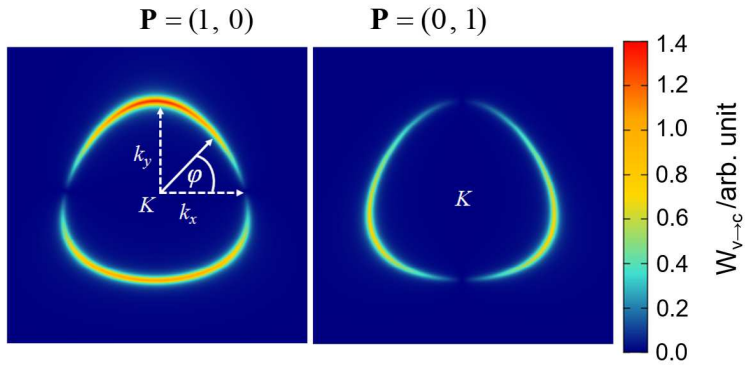

Figure 2.10 Transition probability in Brillouin zone of graphene for $\mathbf{P} = (1, 0)$ and $\mathbf{P} = (0, 1)$ around K point $(4\pi/3a, 0)$. In former (later) case, the nodes are observed at $\varphi = 0, \pi, 2\pi...(\varphi = \pi/2, 3\pi/2...)$.

In Chapter 4, we shall demonstrate that the transition probability in near-field case is determined by the change of electron wave vector in the transition from valence band to conduction band.

Chapter 3

Near-field Enhancement around Metallic Nano-tips

3.1 Parabolic Au Tip

In this chapter, we calculate the near-field enhancement around Au tip placed in vacuum tip with finite-difference method. To perform the calculation, we are required to specify the geometry of the tip as well as its relative permittivity as the function wavelength of irradiating light. We shall show that magnitude of response near-field are mainly determined by these two factors, and therefore enable us to maximize the near-field enhancement by choosing particular tip shape and wavelength of the light.

The relative permittivity of bulk Au is considered as the summation of Drude and Drude-Lorentz terms to include both optical properties originating from intraband and interband transitions of electrons,respectively. As explained in the previous chapter, relative permittivity ϵ_r which includes both terms is expressed as:

$$\epsilon_r(\omega) = \epsilon_\infty - \frac{{\omega_{\mathrm{D}}}^2}{\omega^2 + i\Gamma_{\mathrm{D}}\omega} - \Delta\epsilon\frac{\omega_{\mathrm{L}}^2}{(\omega^2 - \omega_{\mathrm{L}}^2) + i\Gamma_{\mathrm{L}}\omega}. \tag{3.1}$$

The fitting values of parameters in Eq.(3.1) are given in Tab. 3.1. Here the parameter $\Delta\epsilon$ can be interpreted as a weighing factor [69] of the Drude-Lorentz term. These values are applicable to describe the relative permittivity of Au for optical wavelength in the range of 500-1000 nm [69]. The Au tip is modelled as a paraboloid of which the radius of curvature at its apex is denoted by a. Geometry of the tip in the two-dimensional finite-difference calculation domain (xz plane) is depicted in Fig. 3.1.

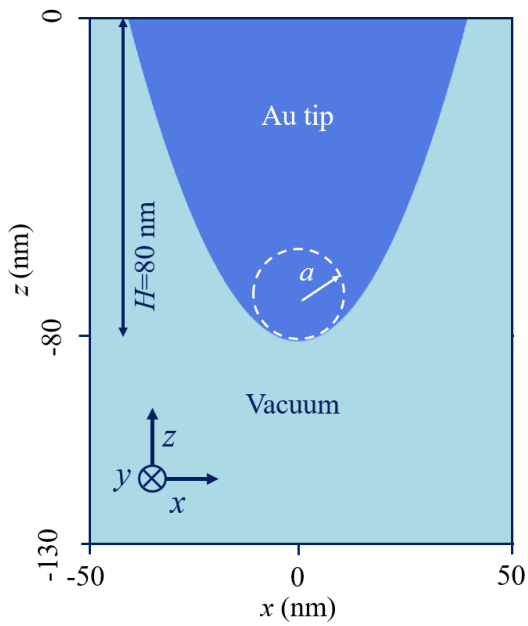

Figure 3.1 Parabolic Au tip in the two-dimensional finite-difference calculation domain (xz) plane, the radius of curvature at tip apex is denoted as a .

ϵ_∞	$\omega_D/2\pi$ (THz)	$\Gamma_D/2\pi$ (THz)	$\omega_L/2\pi$ (THz)	$\Gamma_L/2\pi$ (THz)	$\Delta\epsilon$
5.9673	2113.6	15.92	650.07	104.86	1.09

Table 3.1: Fitting values of parameters contained in the Drude and Drude-Lorentz terms given by Equation 3.1, adapted from reference [69].

The fixed height of the tip H is choosen as 80 nm. This distance is approximately corresponds to the Rayleigh length for the shortest wavelength used in the calculation (500 nm/2π). Because in nano-scale regime the electron-surface scattering effect is not negligible, the damping constants in Drude and Drude-Lorentz terms are modified by using Eqs. (2.21)-(2.23). This modification is explicitly stated as:

$$\Gamma_{D(L)} \rightarrow \Gamma_{D(L)} + A v_F \frac{S}{4V}, \tag{3.2}$$

where S and V are the surface area and volume of the tip, respectively. By using $A = 0.33$ [46] and $v_F = 1.41 \times 10^{15}\text{nm.s}^{-1}$ [55], relative permittivity of the tip ϵ_r is

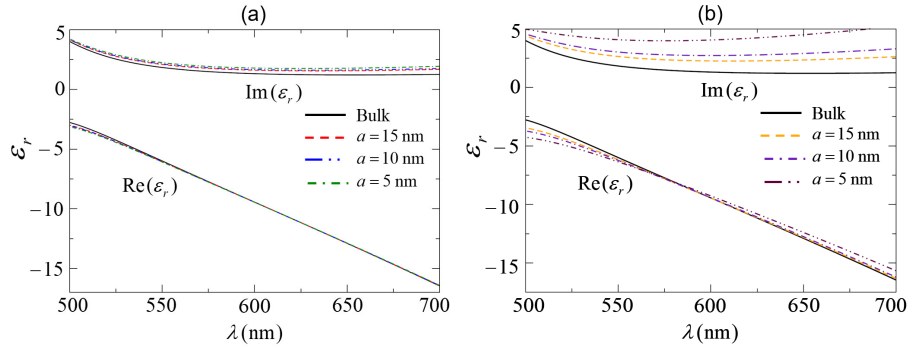

Figure 3.2 Calculated real and imaginary parts of Au in the case of (a) parabolic tip and (b) sphereical nanoparticle whose radius a=5, 10, and 15 nm.

calculated for the optical wavelength λ=500-700 nm. The corresponding calculations are carried out for a=5, 10, and 15 nm in order to capture the size effect on the relative permittivity for the case of parabolic nano-tips and nano-sphere for comparison. The results are presented in Fig. 3.2(a), which shows the increase of the imaginary part of nano-tip relative permittivity as its radius descreases, particularly in the long wavelength region. This property is also observed for the case of spherical nanoparticles as given in (b). The main difference is that the imaginary part of permittivity of nano-sphere increases more quickly compared with the case of parabolic tip, because for a given radius a, the former is less voluminous and the effect of electron-surface boundary scattering is more noticeable in the smaller nanostructure.

The calculation of near-field enhancement distribution around Au nano-tip in the vacuum is then performed numerically with finite difference method. The two-dimensional calculation domain (xz plane) whose size is (100 nm $\times$ 130 nm) is descretized into 1000 $\times$ 1300 square meshes, which means that the size of individual mesh is 0.1 nm$\times$0.1 nm. Hereafter we write (x_i, z_k) to denote a spatial position in the two-dimensional finite-difference domain. Further, we need to assign the appropiate values of electrostatic potentials inside and outside tip at the zeroth iteration (n=0). As has been explained in the Chapter 1, the electric field enhancement is optimized when the electric field emanating from the light $\mathbf{E}_0$ is polarized parallel to the tip axis, and therefore in this work we only consider the corresponding case. Outside the tip, $\mathbf{E}_0$ generates the electrostatic potential $V(\mathbf{r})$ which is equal to $\mp zE_0$, where $\mp$ sign in

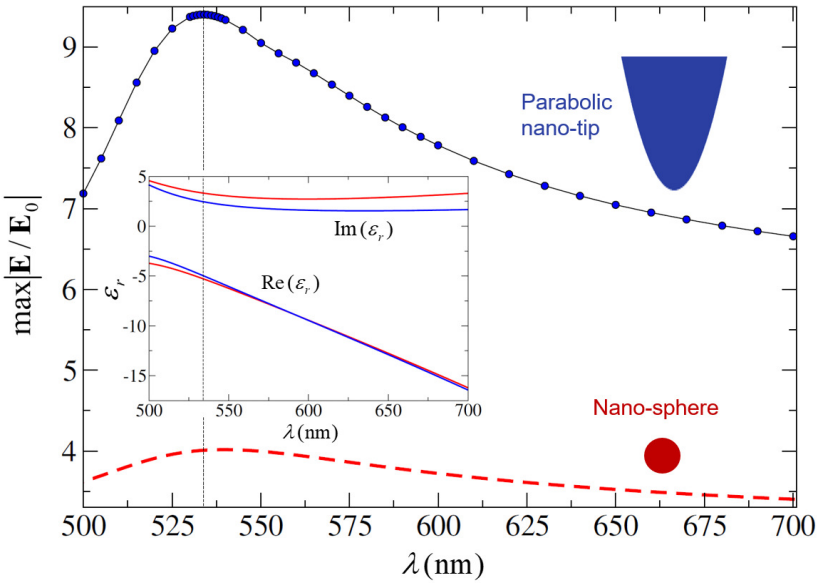

Figure 3.3 Calculated maximum near-field enhancement as the function of irradiating wavelength λ=500-700 nm for Au parabolic tip and spherical nanoparticle. Inset: the optical relative permittivity $\epsilon_r(\lambda)$ of Au parabolic tip (blue) and sphere (red) of radius a=10 nm . Black line intersects the value of maximum enhancement and ϵ_r at $\lambda \approx 534$ nm.

the potential represents $\mathbf{E}_0$ is directed toward $\pm z$ direction. Inside the tip, the value of potential $V(\mathbf{r})$ is zero at n=0, since initially the tip is not affected by $\mathbf{E}_0$. The relative permittivity of the tip at a given wavelength ϵ_r is evaluated by using Eqs. 3.1 and 3.2. The initial conditions of finite-difference calculation are summarized as follows:

$$\text{(Inside tip)} \begin{cases} V_{i,k}^{(n=0)}(\mathbf{r}) & = 0, \\ \epsilon_{i,k}(\mathbf{r},\lambda) & = \epsilon_r(\lambda). \end{cases} \quad \text{(Outside tip)} \begin{cases} V_{i,k}^{(n=0)}(\mathbf{r}) & = \mp E_0 z_k, \\ \epsilon_{i,k}(\mathbf{r},\lambda) & = 1. \end{cases} \tag{3.3}$$

With the previously described procedures, we calculate the near-field enhancement in the vicinity of Au parabolic tip (a=10 nm) for several optical wavelengths to obtain the magnitude of maximum enhancement as the function of wavelength of illuminating light in the range of λ=500-700 nm. For each case, the incoming electric field $\mathbf{E}_0$ is in the $+z$-direction. The finite-difference calculation is performed with iteration number $n = 2.5 \times 10^4$. The result is presented by the blue dots in Fig. 3.3, showing that the resonance condition, i.e. maximum magnitude of near-field enhancement ($\sim$ 9.4) is attained at $\lambda \approx$534 nm. We compare our numerical calculation with the maximum near-field enhancement around the quasi-static sphere, analytically evaluated using

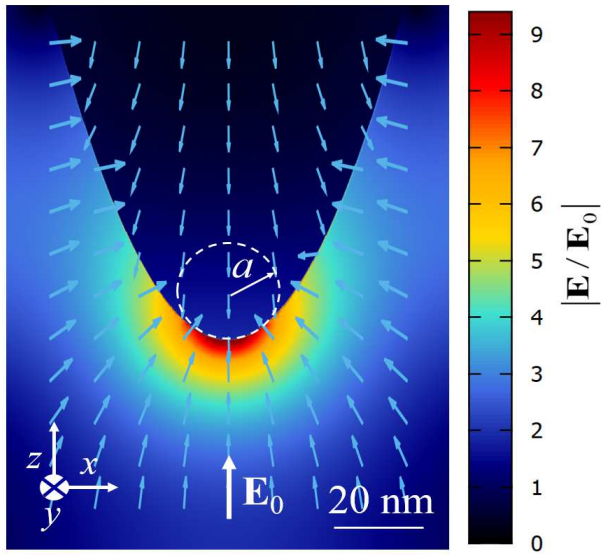

Figure 3.4 Calculated near-field enhancement in the vicinity of parabolic tip (a=10 nm) at excitation wavelength $\lambda \approx$534 nm.

Eqs. (2.55), which is depicted by dashed red line in the figure. The maximum enhancement factor for the case of Au nano-sphere occurs at $\lambda \approx$539.5 nm. Because the resonance conditions are almost overlapping, therefore, its is concluded enhancement in the case of the tip corresponds to the dipole mode of near-field excitation. However, it is also shown that the resonance condition of near-field enhancement in the parabolic tip is slightly blue-shifted (which means that it occurs at smaller wavelength) compared with the nano-sphere. This effect mainly due to the shape-dependence of relative permittivity. It is interesting to compare our results with the Mie theory calculations by Olson et al. [23] on the wavelength dependence of extinction cross section for the individual Au spherical nanoparticle, which show peaks of cross-sections in the Fig. 1.2 appear in almost similar range of optical wavelength. In Fig. 3.4 we show the near-field enhancement of around parabolic tip (a=10 nm) at $\lambda \approx$534 nm, in which arrows represent the directions of the total electric field. The figure indicates that the maximum enhancement occurs below the tip apex, which is dominated by the z-component of the near-field, and the direction of electric field inside the tip is opposite of the direction of incoming field $\mathbf{E}_0$. This result can be explained by the electrostatic lightning rod effect, in which the incoming field induces the Au electron cloud to move

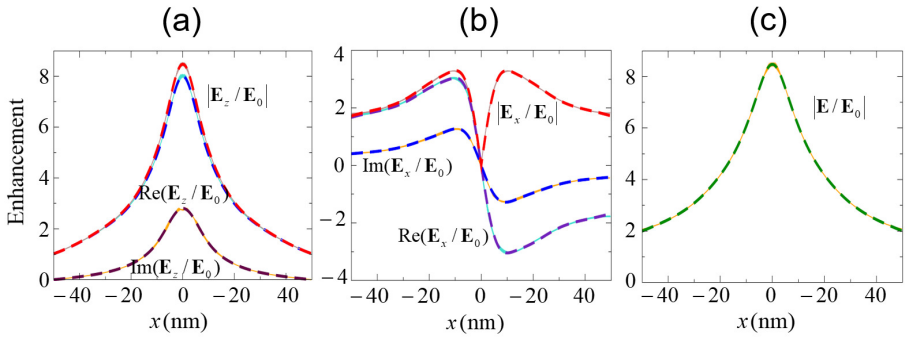

Figure 3.5 Enhancements of (a) z, (b) x, and (c) total components of near-field as the function of x at 2 nm below Au tip apex. Solids and dashed lines represent calculated results using finite-difference method and fitting functions, respectively.

to the opposite end of the tip and in return generates the near-field enhancement.

The distribution of the near-field components at some particular distance below the tip $z = z_0$ is then evaluated to obtain their profiles, which are fitted into Gaussian-based functions. In the Fig. 3.5 (a), (b), and (c) we correspondingly show the profile of z, x, and total near-field components at 2 nm below the tip apex calculated by finite difference method as well as the respective fitting functions. The complex fitting functions are given by:

$$\mathbf{E}_z(x, z = z_0) = E_0 \left(K + \sum_{a=1} A_a e^{\frac{-x^2}{2v_a^2}} + iL + i \sum_{b=1} B_b e^{\frac{-x^2}{2w_b^2}} \right) \hat{\mathbf{z}}, \tag{3.4}$$

$$\mathbf{E}_x(x, z = z_0) = - E_0 x \left(\sum_{c=1} C_c e^{\frac{-x^2}{2f_c^2}} + i \sum_{d=1} D_d e^{\frac{-x^2}{2g_d^2}} \right) \hat{\mathbf{x}}. \tag{3.5}$$

In (a) the width of near-field enhancement magnitude of z component $|\mathbf{E}_z/\mathbf{E}_0|$ is approximately 5.08 nm, while in (b), the near-field enhancement magnitude of x component $|\mathbf{E}_x/\mathbf{E}_0|$ is maximum at $x = \sim \pm 9.75$ nm and eventually vanishes as $x \to \pm\infty$. In (c), by using $|\mathbf{E}| = \sqrt{\mathbf{E}_z^2 + \mathbf{E}_x^2}$, it is found that the width of near-field enhancement magnitude of total components $|\mathbf{E}/\mathbf{E}_0|$ tip is around 5.54 nm, which is only slightly larger compared with that of the z component. By considering the azimuthal symmetry, it is possible to extend the previous fitting method into the calculation of near-field planar distribution on the xy plane. In this consideration, the z, x and y near-field

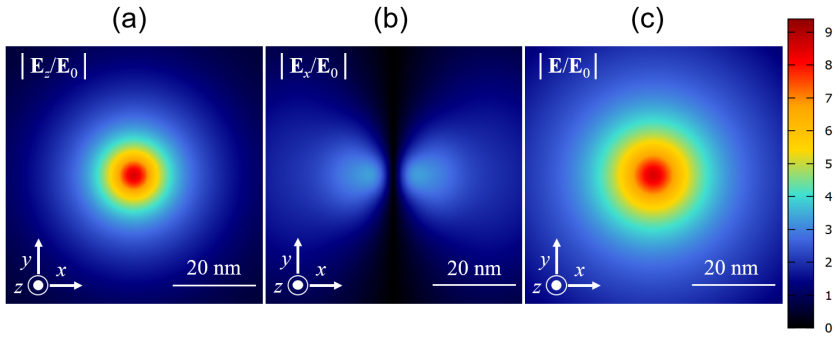

Figure 3.6 Planar distribution (a) z, (b) x and (c) all components of near-field at 2 nm below the Au tip.

components can be written as:

$$\mathbf{E}_z(x,y) = E_0\boldsymbol{\eta}_z(x,y) = E_0\left(K + \sum_{a=1} A_a e^{\frac{-x^2-y^2}{2v_a^2}} + iL + i\sum_{b=1} B_b e^{\frac{-x^2-y^2}{2w_b^2}}\right)\hat{\mathbf{z}}, \tag{3.6}$$

$$\mathbf{E}_x(x,y) = E_0\boldsymbol{\eta}_x(x,y) = -E_0 x\left(\sum_{c=1} C_c e^{\frac{-x^2-y^2}{2f_c^2}} + i\sum_{d=1} D_d e^{\frac{-x^2-y^2}{2g_d^2}}\right)\hat{\mathbf{x}}, \tag{3.7}$$

$$\mathbf{E}_y(x,y) = E_0\boldsymbol{\eta}_y(x,y) = -E_0 y\left(\sum_{c=1} C_c e^{\frac{-x^2-y^2}{2f_c^2}} + i\sum_{d=1} D_d e^{\frac{-x^2-y^2}{2g_d^2}}\right)\hat{\mathbf{y}}. \tag{3.8}$$

In Fig. 3.6 (a), (b), and (c) we respectively depict the enhancement distributions of total, z, and x components of near-field on xy for the corresponding conditions.

In short, we have demonstrated that the wavelength dependence of near-field response for the parabolic Au tip shares almost similar characteristics with the case of quasi-static spherical particle, and the mechanism responsible for the near-field enhancement around the tip corresponds to electrostatic lighting rod effect, which occurs due the concentration of charges in the sharp end of the tip. The charge density accumulated in tip apex is obviously related to geometry of the tip. This lead us to consider another tip shape to optimize the near-field enhancement which is one of the utmost importance in near-field spectroscopy.

3.2 Conical Au Tip

Now we calculate the near-field enhancement for the case of conical tip as an alternative shape to obtain larger near-field enhancement compared with the case of parabolic tip.

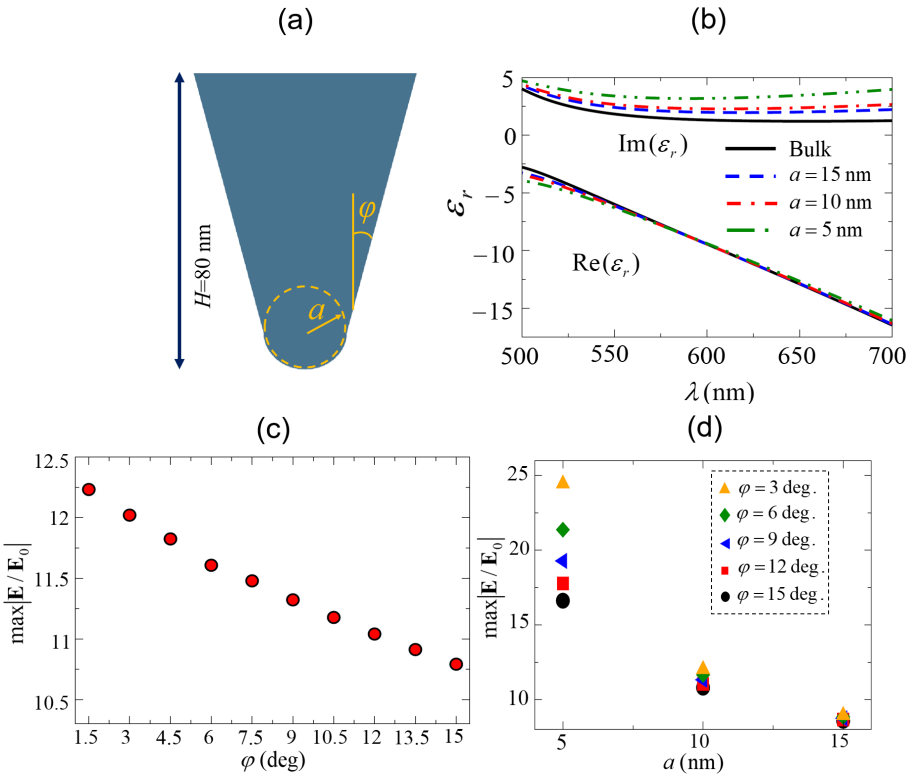

Figure 3.7 (a) Geometrical depiction of the conical tip, (b) The relative permittivity of Au tip ϵ_r corresponds to φ=15 deg for a=15, 10, and 5 nm. The calculated magnitudes of near-field enhancement as the function of (c) φ and fixed a=10 nm, and (d) for a=15, 10, and 5 nm and φ=15, 12, 9, 6, and 3 degree.

Geometry of the tip is described as an upside-down truncated cone with hemisphere of radius a at its bottom, where the angle between its slant and z axis is φ, and as in the previous calculations, the height of tip H is 80 nm. The shape of conical tip is illustrated in Fig. 3.7(a). The size effect on the relative permittivity $\epsilon_r(\lambda)$ of conical Au tip (φ=15 deg.) is presented in (b), which shows more rapid increases of its imaginary part as the tip radius decreases in the long wavelength regime compared with the case of parabolic tip. The reason for this property is because for a given radius a, the conical tip possesses more surface-to-volume ratio compared to to parabolic tip of the identical radius, and therefore, the electron-surface scattering effect on ϵ_r is more pronounced in the former case. With the finite-difference procedures applied for the parabolic tip, we calculate the magnitude of maximum near-field enhancement factor

$|\mathbf{E}/\mathbf{E}_0|$ as the functions of two geometrical parameters of conical tip, namely opening angle φ and radius a. We assume that the wavelength dependence of $|\mathbf{E}/\mathbf{E}_0|$ is similar to the case of parabolic tip, and for this reason, the corresponding calculations are performed only for $\lambda \approx$534 nm. The magnitude of maximum enhancement factor the function of φ (a=10 nm) is presented in (c) which shows monotonic growth of $|\mathbf{E}/\mathbf{E}_0|$ as φ becomes smaller. In (d) we calculate $|\mathbf{E}/\mathbf{E}_0|$ by choosing a=15, 10, and 5 nm for φ=15, 12, 9, 6, and 3 degree, in which the smaller radius of the tip yields larger magnitude of near-field enhancement factor. The results from (c) and (d) are again the direct implications of the lightning-rod effect, where the induced surface charge density accumulated around the tip apex is becomes higher as both φ and a decrease.

As a resume, we have shown that although the near-field response of the nano-tips are almost similar to the quasi-static sphere, of which for many practical purposes the nano-tips are often approximated. However, the finite-difference calculations reveal some aspects of near-field enhancement properties that can not be accounted by the quasi-static sphere model. For example, it is demonstrated that beside complex relative permittivities of the tip and the surrounding medium $\epsilon_r(\lambda)$, tip shape and the related geometrical parameters plays definitive role in determining the magnitude of near-field enhancement factor in its vicinity, while the spherical quasi-static model predicts the size invariance of the near-field enhancement factor, as described by Eq. (2.55).

3.3 Comparison with Calculations from Some Established Works

At the end of this chapter, we perform two calculations of the near-field enhancement around nano-tips which were established in some works. This is done because (1) we need verify the accuracy of our finite-difference method and its comparison with the calculations using other techniques, such as finite-element (FE) and finite-difference time-domain (FDTD) methods which numerically solve the Maxwell equations rather than much simpler the Laplace equation, and (2) to obtain some information on the magnitude near-field enhancement around materials made other than Au at some particular optical wavelength.

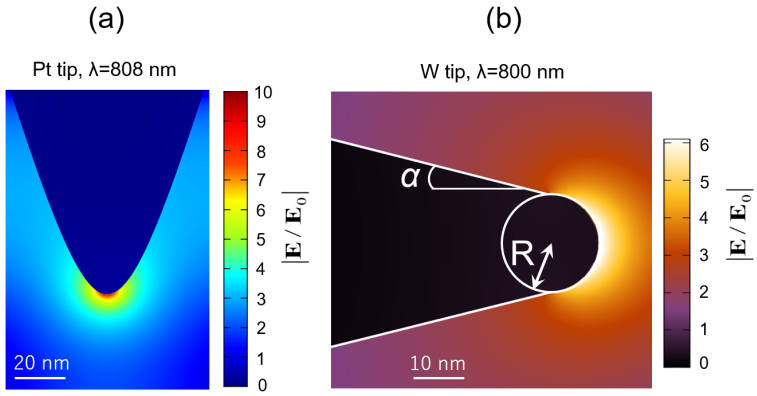

Figure 3.8 Finite-difference calculation of near-field enhancements in the vicinity of (a) Pt tip at λ=808 nm and (b) W tip (R=10 nm, α=15 degree) at λ=800 nm. In both calculations the direction of incoming electric field $\mathbf{E}_0$ is parallel to tip axis.

The FE simulation of near-field enhancement around Pt tip under the irradiation by the laser of wavelength λ=808 nm by Cui et al. [25] ($\epsilon_{\text{tip}} = -17.179+29.609i$) is given in Fig. 1.5(a), while in (b) the FTDT calculation of near-field enhancement around W tip shined by light of wavelength 800 nm by Thomas et al. [26] ($\epsilon_{\text{tip}} \sim 5+i19i$) is depicted. In Fig. 3.8 we present reproduction of the two calculations, performed with the quasi-static finite-diffrerence method, where it can be observed that maximum magnitude of near-field enhancements in (a) and (b) are ~ 10 and ~ 6.1, respectively. Referring to Fig 1.5, it is inferred that our results are in good agreement with one obtained in the corresponding works, and therefore to some extent justify the applicability of our finite-difference method for the calculation of near-field enhancement around metallic nano-tips.

Chapter 4

Near-Field Induced Optical Transition in Graphene

In this chapter, we discuss the effect of the near-field around Au tip on the optical transition of an electron in graphene, which occurs from valence band to conduction band. The near-field induced optical transition is interpreted from the results of optical matrix element calculations for the near-field. After calculating the optical matrix element, we describes the properties transition probability affected by near-field in graphene.

4.0.1 Near-Field Optical Matrix Element

We begin the story by describing the general expression of the far-field optical matrix element, because it shall be shown later that the description the coupling between of near-field and electron in graphene can be expressed in the term of the far-field optical matrix element. In the origin of Cartesian coordinate, $2p_z$ orbital of graphene in Eq. (**??**) is written by

$$\varphi(\mathbf{R},\mathbf{z}) = \varphi(\mathbf{x},\mathbf{y},\mathbf{z}) = z\sum_{k=1}^{4} I_k \exp\left[\frac{-x^2-y^2-z^2}{2\sigma_k^2}\right]. \tag{4.1}$$

We introduce the shift constants $\alpha = \alpha(\sigma_k)$ and $\beta = \beta(\sigma_k)$ for a given σ_k and transform the coordinates $x \to x - \alpha$ and $y \to y - \beta$. The reason for this coordinates shifting is to simplify the integration as shown below. The gradient of the wave function after

the transformations is given by

$$\nabla\varphi(\mathbf{x}-\alpha\hat{\mathbf{x}},\mathbf{y}-\beta\hat{\mathbf{y}},\mathbf{z})=\varphi(\mathbf{x},\mathbf{y},\mathbf{z})\left[\frac{\alpha-x}{\sigma_k^2}\hat{\mathbf{x}}+\frac{\beta-y}{\sigma_k^2}\hat{\mathbf{y}}+\frac{z^{-1}-z}{\sigma_k^2}\hat{\mathbf{z}}\right] \tag{4.2}$$

Let we define the vectorial matrix element $\mathbf{m}_{\text{opt}}^{\text{A}}$ which is is defined as $\langle\varphi(\mathbf{r}-\boldsymbol{\delta}_n^{\text{A}})|\nabla|\varphi(\mathbf{r})\rangle$, let us remind the readers that $\boldsymbol{\delta}_n^{\text{A}},\ n=1,2,3$ are the nearest-neighbour vectors connecting carbon atom in A sublattice to its three nearest neighbour atoms in B sublattice, as has been defined in the Chapter 2. By using Eq. (4.2) we have

$$\begin{aligned}\mathbf{m}_{\text{opt}}^{\text{A}}=&\int_{-\infty}^{\infty}\mathrm{d}v\ z\sum_{l=1}^{4}I_l e^{(\frac{-x^2-y^2-z^2}{2\sigma_l^2})}\nabla\left[z\sum_{k=1}^{4}I_k e^{(\frac{-x^2-y^2-z^2}{2\sigma_k^2})}\right]\\&\int_{-\infty}^{\infty}\mathrm{d}v\Bigg(\varphi(\mathbf{x}-\alpha\hat{\mathbf{x}}-\mathbf{x}_n^{\text{A}},\mathbf{y}-\beta\hat{\mathbf{y}}-\mathbf{y}_n^{\text{A}},z)\left[\frac{\alpha-x}{\sigma_k^2}\hat{\mathbf{x}}+\frac{\beta-y}{\sigma_k^2}\hat{\mathbf{y}}+\frac{z^{-1}-z}{\sigma_k^2}\hat{\mathbf{z}}\right]\times\\&\varphi(\mathbf{x}-\alpha\hat{\mathbf{x}},\mathbf{y}-\beta\hat{\mathbf{y}},\mathbf{z})\Bigg),\end{aligned} \tag{4.3}$$

where $\mathbf{x}_n^{\text{A}}$ and $\mathbf{y}_n^{\text{A}}$ are respectively the x and y components of vector $\boldsymbol{\delta}_n^{\text{A}}$, and the integration is performed over volume element $\mathrm{d}v=\mathrm{d}x\mathrm{d}y\mathrm{d}z$. The integration which consists the third term in square bracket in Eq. (4.3) vanishes since the integrand is an odd function with respect to z. The integral of remaining terms are calculated as follows:

$$\begin{aligned}\mathbf{m}_{\text{opt}}^{\text{A}}=&\sum_{l=1}^{4}\sum_{k=1}^{4}\left[\int_{-\infty}^{\infty}\mathrm{d}z\ z^2e^{-\frac{z^2}{2}(\frac{1}{\sigma_k^2}+\frac{1}{\sigma_l^2})}\right]\left[\int_{-\infty}^{\infty}\mathrm{d}y\ e^{-\frac{y^2}{2}(\frac{1}{\sigma_k^2}+\frac{1}{\sigma_l^2})}e^{y(\frac{\beta}{\sigma_k^2}+\frac{\beta+y_n^{\text{A}}}{\sigma_l^2})}\right]\times\\&\left[\int_{-\infty}^{\infty}\mathrm{d}x\ e^{-\frac{x^2}{2}(\frac{1}{\sigma_k^2}+\frac{1}{\sigma_l^2})}e^{x(\frac{\alpha}{\sigma_k^2}+\frac{\alpha+x_n^{\text{A}}}{\sigma_l^2})}\frac{\alpha-x}{\sigma_k^2}\right]\times\\&\left[e^{\frac{-\alpha^2-\beta^2}{2\sigma_k^2}}e^{-\frac{(\alpha+x_n^{\text{A}})}{2\sigma_l^2}}e^{-\frac{(\beta+y_n^{\text{A}})}{2\sigma_l^2}}\right]\hat{\mathbf{x}}+\\&\left[\int_{-\infty}^{\infty}\mathrm{d}z\ z^2e^{-\frac{z^2}{2}(\frac{1}{\sigma_k^2}+\frac{1}{\sigma_l^2})}\right]\left[\int_{-\infty}^{\infty}\mathrm{d}x\ e^{-\frac{x^2}{2}(\frac{1}{\sigma_k^2}+\frac{1}{\sigma_l^2})}e^{x(\frac{\alpha}{\sigma_k^2}+\frac{\alpha+x_n^{\text{A}}}{\sigma_l^2})}\right]\times\\&\left[\int_{-\infty}^{\infty}\mathrm{d}y\ e^{-\frac{y^2}{2}(\frac{1}{\sigma_k^2}+\frac{1}{\sigma_l^2})}e^{y(\frac{\beta}{\sigma_k^2}+\frac{\beta+y_n^{\text{A}}}{\sigma_l^2})}\frac{\beta-y}{\sigma_k^2}\right]\times\\&\left[e^{\frac{-\alpha^2-\beta^2}{2\sigma_k^2}}e^{-\frac{(\alpha+x_n^{\text{A}})}{2\sigma_l^2}}e^{-\frac{(\beta+y_n^{\text{A}})}{2\sigma_l^2}}\right]\hat{\mathbf{y}}\end{aligned} \tag{4.4}$$

In order to avoid over-complicated in the analytical solution, we need to choose some special values for both α and β. This step is permissible because the value of integral over entire space in Eq. (4.3) does not change by shifting the origin into some particular points in the coordinate. The values of α and β are chosen as such so the following relations are satisfied

$$\left(\frac{\alpha}{\sigma_k^2}+\frac{\alpha+x_n^{\mathrm{A}}}{\sigma_l^2}\right)=0,\ \left(\frac{\beta}{\sigma_k^2}+\frac{\beta+y_n^{\mathrm{A}}}{\sigma_l^2}\right)=0, \tag{4.5}$$

which yields

$$\alpha=-\frac{x_n^{\mathrm{A}}}{\sigma_l^2}\left(\frac{1}{\sigma_k^2}+\frac{1}{\sigma_l^2}\right)^{-1},\ \beta=-\frac{y_n^{\mathrm{A}}}{\sigma_l^2}\left(\frac{1}{\sigma_k^2}+\frac{1}{\sigma_l^2}\right). \tag{4.6}$$

Therefore, the constants in Eq. (4.4) are given as follows:

$$e^{\frac{-\alpha^2-\beta^2}{2\sigma_k^2}}e^{-\frac{(\alpha+x_n^{\mathrm{A}})}{2\sigma_l^2}}e^{-\frac{(\beta+y_n^{\mathrm{A}})}{2\sigma_l^2}}=\exp\left[-\frac{a_{\mathrm{CC}}^2}{2}\frac{1}{(\sigma_k^2+\sigma_l^2)^2}\right], \tag{4.7}$$

where $a_{\mathrm{CC}}=|\boldsymbol{\delta}_n^{\mathrm{A}}|$ is the length of nearest-neighbour vectors pointing from atom A to atom B. Continuing the derivation of Eq. (4.7), the optical matrix element is given by

$$\begin{aligned}\mathbf{m}_{\mathrm{opt}}^{\mathrm{A}}=&\sqrt{8\pi^3}\sum_{l=1}^{4}\sum_{k=1}^{4}\left[I_kI_l\,\exp\left[-\frac{a_{\mathrm{CC}}^2}{2}\frac{1}{(\sigma_k^2+\sigma_l^2)^2}\right]\left(\frac{1}{\sigma_k^2}+\frac{1}{\sigma_l^2}\right)^{-5/2}\right]\times\\&\left[\frac{-x_n^{\mathrm{A}}}{\sigma_k^2+\sigma_l^2}\hat{\mathbf{x}}+\frac{-y_n^{\mathrm{A}}}{\sigma_k^2+\sigma_l^2}\hat{\mathbf{y}}\right]\\=&\sqrt{8\pi^3}\sum_{l=1}^{4}\sum_{k=1}^{4}\left[I_kI_l\,\exp\left[-\frac{a_{\mathrm{CC}}^2}{2}\frac{1}{(\sigma_k^2+\sigma_l^2)^2}\right]\left(\frac{1}{\sigma_k^2}+\frac{1}{\sigma_l^2}\right)^{-5/2}\frac{1}{\sigma_k^2+\sigma_l^2}\right](-\boldsymbol{\delta}_n^{\mathrm{A}})\end{aligned} \tag{4.8}$$

From the Eq. (4.8), it is concluded that the direction of $\mathbf{m}_{\mathrm{opt}}^{\mathrm{A}}$ is opposite to the vector connecting carbon atom in sub-lattice A to its three nearest neighbour atoms in sub-lattice B. By similar mathematical arguments, it can be shown that the direction of $\mathbf{m}_{\mathrm{opt}}^{\mathrm{B}}\equiv\langle\varphi(\mathbf{r}-\boldsymbol{\delta}_n^{\mathrm{B}})|\nabla|\varphi(\mathbf{r})\rangle$ is in the direction of $-\boldsymbol{\delta}_n^{\mathrm{B}}$. These results together justify the reasoning which leads to the Eq. (2.102). By using the fitting values provided in Table 2.1, it can be calculated that the magnitude of optical matrix element $|\mathbf{m}_{\mathrm{opt}}^{\mathrm{A}}|=|\mathbf{m}_{\mathrm{opt}}^{\mathrm{B}}|$ is equal to the one claimed in [67].

Now let us calculate near-field induced optical transition of electron in graphene. Let us suppose that a monolayer graphene is placed 2 nm below the parabolic Au

tip apex, of which the near-field distribution on the xy plane at λ ∼534 nm has been calculated in Chapter 3. We consider that the introduction of graphene does not significantly alter the previously calculated result since in the optical wavelength, graphene is almost transparent, for only absorbing 2.3% of the light [32]. The spatial distribution of near-field components on the graphene (xy) plane are fitted into Gaussian-based function given in Eqs. (3.6)-(3.8). Hereafter we adopt the notation for near-field distribution introduced in Eq. (2.103). By recalling tigh-binding wave function of graphene provided by Eqs. (2.87) and (2.88), the following is the explicit form of the electron-near-field matrix element specifying the electron optical transition from valence to conduction bands due to the near-field distribution generated by light frequency ω_{L}:

$$
\begin{aligned}
M_{\mathrm{e-nf}}(\mathbf{k}_i,\mathbf{k}_f) = \sum_{\sigma=x,y,z}\frac{1}{N}\sum_{j=1}^{N}\sum_{j'=1}^{N}\frac{e\hbar}{m\omega}E_0 e^{i(\omega_f-\omega_i\pm\omega_{\mathrm{L}})}\times \\
\Big[C_{\mathrm{A}}^{\mathrm{c}*}(\mathbf{k}_f)C_{\mathrm{A}}^{\mathrm{v}}(\mathbf{k}_i)e^{i(\mathbf{k}_i\cdot\mathbf{R}_j^{\mathrm{A}}-\mathbf{k}_f\cdot\mathbf{R}_{j'}^{\mathrm{A}})}\langle\varphi(\mathbf{z},\mathbf{R}-\mathbf{R}_{j'}^{\mathrm{A}})|\boldsymbol{\eta}_\sigma(\mathbf{R})\cdot\nabla|\varphi(\mathbf{z},\mathbf{R}-\mathbf{R}_j^{\mathrm{A}})\rangle+ \\
C_{\mathrm{A}}^{\mathrm{c}*}(\mathbf{k}_f)C_{\mathrm{B}}^{\mathrm{v}}(\mathbf{k}_i)e^{i(\mathbf{k}_i\cdot\mathbf{R}_j^{\mathrm{B}}-\mathbf{k}_f\cdot\mathbf{R}_{j'}^{\mathrm{A}})}\langle\varphi(\mathbf{z},\mathbf{R}-\mathbf{R}_{j'}^{\mathrm{A}})|\boldsymbol{\eta}_\sigma(\mathbf{R})\cdot\nabla|\varphi(\mathbf{z},\mathbf{R}-\mathbf{R}_j^{\mathrm{B}})\rangle+ \\
C_{\mathrm{B}}^{\mathrm{c}*}(\mathbf{k}_f)C_{\mathrm{A}}^{\mathrm{v}}(\mathbf{k}_i)e^{i(\mathbf{k}_i\cdot\mathbf{R}_j^{\mathrm{A}}-\mathbf{k}_f\cdot\mathbf{R}_{j'}^{\mathrm{B}})}\langle\varphi(\mathbf{z},\mathbf{R}-\mathbf{R}_{j'}^{\mathrm{B}})|\boldsymbol{\eta}_\sigma(\mathbf{R})\cdot\nabla|\varphi(\mathbf{z},\mathbf{R}-\mathbf{R}_j^{\mathrm{A}})\rangle+ \\
C_{\mathrm{B}}^{\mathrm{c}*}(\mathbf{k}_f)C_{\mathrm{B}}^{\mathrm{v}}(\mathbf{k}_i)e^{i(\mathbf{k}_i\cdot\mathbf{R}_j^{\mathrm{B}}-\mathbf{k}_f\cdot\mathbf{R}_{j'}^{\mathrm{B}})}\langle\varphi(\mathbf{z},\mathbf{R}-\mathbf{R}_{j'}^{\mathrm{B}})|\boldsymbol{\eta}_\sigma(\mathbf{R})\cdot\nabla|\varphi(\mathbf{z},\mathbf{R}-\mathbf{R}_j^{\mathrm{B}})\rangle\Big]
\end{aligned}
\tag{4.9}
$$

The long expression in the Eq. (4.9) can be simplified by introducing two auxiliary the coordinates

$$\mathbf{R'} \equiv \mathbf{R}-\mathbf{R}_j^{\mathrm{A}}, \tag{4.10}$$

$$\mathbf{R''} \equiv \mathbf{R}-\mathbf{R}_j^{\mathrm{B}}. \tag{4.11}$$

Then these two coordinates can be interpreted as the relative position of A and B carbon atoms relative to the centre of the tip at xy plane,respectively. By substituting $\mathbf{R}\rightarrow\mathbf{R'}$ ($\mathbf{R}\rightarrow\mathbf{R''}$) in first and third (second and fourth) terms in the square bracket of the Eq. (4.9), as well as performing some algebraic manipulation in the complex

exponential terms of the same equation, hence

$$M_{\mathrm{e-nf}}(\mathbf{k}_i,\mathbf{k}_f)=\sum_{\sigma=x,y,z}\frac{1}{N}\sum_{j=1}^{N}\sum_{j'=1}^{N}\frac{e\hbar}{m\omega}E_0e^{i(\omega_f-\omega_i\pm\omega_{\mathrm{L}})}\times$$

$$\Big[C_{\mathrm{A}}^{\mathrm{c}*}(\mathbf{k}_f)C_{\mathrm{A}}^{\mathrm{v}}(\mathbf{k}_i)e^{i(\mathbf{k}_i-\mathbf{k}_f)\cdot\mathbf{R}_j^{\mathrm{A}}}e^{i\mathbf{k}_f\cdot(\mathbf{R}_j^{\mathrm{A}}-\mathbf{R}_{j'}^{\mathrm{A}})}\langle\varphi(\mathbf{z},\mathbf{R'}+\mathbf{R}_j^{\mathrm{A}}-\mathbf{R}_{j'}^{\mathrm{A}})|\boldsymbol{\eta}_\sigma(\mathbf{R'}+\mathbf{R}_j^{\mathrm{A}})\cdot\nabla|\varphi((\mathbf{z},\mathbf{R'})\rangle+$$

$$C_{\mathrm{A}}^{\mathrm{c}*}(\mathbf{k}_f)C_{\mathrm{B}}^{\mathrm{v}}(\mathbf{k}_i)e^{i(\mathbf{k}_i-\mathbf{k}_f)\cdot\mathbf{R}_j^{\mathrm{B}}}e^{i\mathbf{k}_f\cdot(\mathbf{R}_j^{\mathrm{B}}-\mathbf{R}_{j'}^{\mathrm{A}})}\langle\varphi((\mathbf{z},\mathbf{R''}+\mathbf{R}_j^{\mathrm{B}}-\mathbf{R}_{j'}^{\mathrm{A}})|\boldsymbol{\eta}_\sigma(\mathbf{R''}+\mathbf{R}_j^{\mathrm{B}})\cdot\nabla|\varphi((\mathbf{z},\mathbf{R''})\rangle+$$

$$C_{\mathrm{B}}^{\mathrm{c}*}(\mathbf{k}_f)C_{\mathrm{A}}^{\mathrm{v}}(\mathbf{k}_i)e^{i(\mathbf{k}_i-\mathbf{k}_f)\cdot\mathbf{R}_j^{\mathrm{A}}}e^{i\mathbf{k}_f\cdot(\mathbf{R}_j^{\mathrm{A}}-\mathbf{R}_{j'}^{\mathrm{B}})}\langle\varphi((\mathbf{z},\mathbf{R'}+\mathbf{R}_j^{\mathrm{A}}-\mathbf{R}_{j'}^{\mathrm{B}})|\boldsymbol{\eta}_\sigma(\mathbf{R'}+\mathbf{R}_j^{\mathrm{A}})\cdot\nabla|\varphi(\mathbf{z},\mathbf{R'})\rangle+$$

$$C_{\mathrm{B}}^{\mathrm{c}*}(\mathbf{k}_f)C_{\mathrm{B}}^{\mathrm{v}}(\mathbf{k}_i)e^{i(\mathbf{k}_i-\mathbf{k}_f)\cdot\mathbf{R}_j^{\mathrm{B}}}e^{i\mathbf{k}_f\cdot(\mathbf{R}_j^{\mathrm{B}}-\mathbf{R}_{j'}^{\mathrm{B}})}\langle\varphi((\mathbf{z},\mathbf{R''}+\mathbf{R}_j^{\mathrm{B}}-\mathbf{R}_{j'}^{\mathrm{B}})|\boldsymbol{\eta}_\sigma(\mathbf{R''}+\mathbf{R}_j^{\mathrm{B}})\cdot\nabla|\varphi((\mathbf{z},\mathbf{R''})\rangle\Big]. \tag{4.12}$$

The next step is performing summation with respect to lattice index j', and since we only consider the nearest-neighbour interactions, the subtraction of $\mathbf{R}_j^{\mathrm{A}}-\mathbf{R}_{j'}^{\mathrm{B}}$ and $\mathbf{R}_j^{\mathrm{B}}-\mathbf{R}_{j'}^{\mathrm{A}}$ will respectively yield the three nearest-neighbour vectors $\boldsymbol{\delta}_n^{\mathrm{A}}$ and $\boldsymbol{\delta}_n^{\mathrm{B}}$, $n=1,2,3$ while $\mathbf{R}_j^{\mathrm{A}}-\mathbf{R}_{j'}^{\mathrm{A}}=\mathbf{R}_j^{\mathrm{B}}-\mathbf{R}_{j'}^{\mathrm{B}}=0$ because the subtracted vectors point to the similar site of carbon atom in the graphene plane. By defining $\Delta\mathbf{k}\equiv\mathbf{k}_f-\mathbf{k}_i$ as the change of electron momentum from valence to conduction band, Eq. (4.12) is thus reduced to

$$M_{\mathrm{e-nf}}(\mathbf{k}_i,\mathbf{k}_f)=\sum_{\sigma=x,y,z}\frac{1}{N}\sum_{j=1}^{N}\frac{e\hbar}{m\omega}E_0e^{i(\omega_f-\omega_i\pm\omega_{\mathrm{L}})}\times$$

$$\Big[C_{\mathrm{A}}^{\mathrm{c}*}(\mathbf{k}_f)C_{\mathrm{A}}^{\mathrm{v}}(\mathbf{k}_i)e^{-i\Delta\mathbf{k}\cdot\mathbf{R}_j^{\mathrm{A}}}\langle\varphi(\mathbf{z},\mathbf{R'})|\boldsymbol{\eta}_\sigma(\mathbf{R'}+\mathbf{R}_j^{\mathrm{A}})\cdot\nabla|\varphi(\mathbf{z},\mathbf{R'})\rangle+$$

$$C_{\mathrm{A}}^{\mathrm{c}*}(\mathbf{k}_f)C_{\mathrm{B}}^{\mathrm{v}}(\mathbf{k}_i)e^{-i\Delta\mathbf{k}\cdot\mathbf{R}_j^{\mathrm{B}}}e^{-i\mathbf{k}_f\cdot\boldsymbol{\delta}_n^{\mathrm{B}}}\langle\varphi(\mathbf{z},\mathbf{R''}-\boldsymbol{\delta}_n^{\mathrm{B}})|\boldsymbol{\eta}_\sigma(\mathbf{R''}+\mathbf{R}_j^{\mathrm{B}})\cdot\nabla|\varphi(\mathbf{z},\mathbf{R''})\rangle+$$

$$C_{\mathrm{B}}^{\mathrm{c}*}(\mathbf{k}_f)C_{\mathrm{A}}^{\mathrm{v}}(\mathbf{k}_i)e^{-i\Delta\mathbf{k}\cdot\mathbf{R}_j^{\mathrm{A}}}e^{-i\mathbf{k}_f\cdot\boldsymbol{\delta}_n^{\mathrm{A}}}\langle\varphi(\mathbf{z},\mathbf{R'}-\boldsymbol{\delta}_n^{\mathrm{A}})|\boldsymbol{\eta}_\sigma(\mathbf{R'}+\mathbf{R}_j^{\mathrm{A}})\cdot\nabla|\varphi(\varphi(\mathbf{z},\mathbf{R'})\rangle+$$

$$C_{\mathrm{B}}^{\mathrm{c}*}(\mathbf{k}_f)C_{\mathrm{B}}^{\mathrm{v}}(\mathbf{k}_i)e^{-i\Delta\mathbf{k}\cdot\mathbf{R}_j^{\mathrm{B}}}\langle\varphi(\mathbf{r})|\boldsymbol{\eta}_\sigma(\mathbf{z},\mathbf{R''}+\mathbf{R}_j^{\mathrm{B}})\cdot\nabla|\varphi(\mathbf{z},\mathbf{R''})\rangle\Big]. \tag{4.13}$$

Let us recall that the width of the planar near-field components distribution (around the size of tip diameter $2a$) is considerably larger compared with distance between carbon atoms in graphene, which is 0.142 nm. Therefore, we can regard $\mathbf{R}_j^{\mathrm{A}}\approx\mathbf{R}_j^{\mathrm{A}}=\mathbf{R}_j^u$ in the corresponding equation since the planar near-field distribution on the two atoms in a given unit cell at $\mathbf{R}_j^u$ are almost equal. Hence, Eq. (4.13) is further simplified

by

$$M_{\mathrm{e-nf}}(\mathbf{k}_i,\mathbf{k}_f)=\sum_{\sigma=x,y}\frac{1}{N}\sum_{j=1}^{N}\frac{e\hbar}{m\omega}E_0e^{i(\omega_f-\omega_i\pm\omega_{\mathrm{L}})}\times \\ \Bigg[C_{\mathrm{A}}^{\mathrm{c}*}(\mathbf{k}_f)C_{\mathrm{B}}^{\mathrm{v}}(\mathbf{k}_i)e^{-i\mathbf{k}_f\cdot\boldsymbol{\delta}_n^{\mathrm{B}}}e^{-i\Delta\mathbf{k}\cdot\mathbf{R}_j^{\mathrm{u}}}m_{\mathrm{opt}}^{\sigma}(\mathbf{R}-\mathbf{R}_j^{u})(-\hat{\boldsymbol{\sigma}}\cdot\boldsymbol{\delta}_n^{\mathrm{B}})+ \\ C_{\mathrm{B}}^{\mathrm{c}*}(\mathbf{k}_f)C_{\mathrm{A}}^{\mathrm{v}}(\mathbf{k}_i)e^{-i\mathbf{k}_f\cdot\boldsymbol{\delta}_n^{\mathrm{A}}}e^{-i\Delta\mathbf{k}\cdot\mathbf{R}_j^{\mathrm{u}}}m_{\mathrm{opt}}^{\sigma}(\mathbf{R}-\mathbf{R}_j^{u})(-\hat{\boldsymbol{\sigma}}\cdot\boldsymbol{\delta}_n^{\mathrm{A}})\Bigg], \tag{4.14}$$

where

$$\begin{aligned} m_{\mathrm{opt}}^{\sigma}(\mathbf{R}-\mathbf{R}_j^{u}) =&\langle\varphi(\mathbf{z},\mathbf{R}-\boldsymbol{\delta}_n^{\mathrm{A,B}})|\boldsymbol{\eta}_{\sigma}(\mathbf{R}+\mathbf{R}_j^{\mathrm{u}})\cdot\nabla|\varphi(\mathbf{z},\mathbf{R})\rangle \\ =&\hat{\sigma}\cdot\langle\varphi(\mathbf{z},\mathbf{R}-\boldsymbol{\delta}_n^{\mathrm{A,B}})|\eta_{\sigma}(\mathbf{R}+\mathbf{R}_j^{\mathrm{u}})\nabla|\varphi(\mathbf{z},\mathbf{R})\rangle \end{aligned} \tag{4.15}$$

is the **near-field optical matrix element**. By using tight-binding relation given by Eq. (2.95), the first and the last terms in the square bracket of Eq. (4.13) will cancel each other. Since both graphene $2p_z$ orbital and the near-field components distribution on the graphene plane are fitted into Gaussian-based functions as we discussed in Chapters 2 and 3, then calculation of the remaining terms in Eq. (4.13) can be performed analytically. Nevertheless, here we skip the rather tedious derivation and instead provide a qualitative explanation to recompense the necessary quantitative description. Since the width of the planar near-field components distribution is also much larger than the size of graphene $2p_z$ orbital whose size is in order of 0.1 nm, the magnitude of near-field is constant over the individual orbital and hence $m_{\mathrm{opt}}^{\sigma=x,y}(\mathbf{R}-\mathbf{R}_j^{u})$ is proportional to product of the near-field enhancement factor at $\mathbf{R}_j^{\mathrm{u}}$, which is denoted $\eta_{\sigma=x,y}(\mathbf{R}_j^{\mathrm{u}})$, and the far-field optical matrix element m_{opt}, given by

$$m_{\mathrm{opt}}^{\sigma=x,y}(\mathbf{R}-\mathbf{R}_j^{u})\approx\eta_{\sigma=x,y}(\mathbf{R}_j^{\mathrm{u}})m_{\mathrm{opt}}\ . \tag{4.16}$$

Before continuing the discussion, it is noteworthy to mention that the z component of the near-field distribution is zero, i.e.

$$\int_{-\infty}^{\infty}\mathrm{d}v\langle\varphi(\mathbf{r}-\boldsymbol{\delta}_n^{\mathrm{A(B)}})|\eta_z(\mathbf{R}+\mathbf{R}_j^{\mathrm{A(B)}})\nabla|\varphi(\mathbf{r})\rangle=0, \tag{4.17}$$

because the integrands are an odd function with respect to z. Therefore, even though possesses larger enhancement factor compared with the near-field planar components as demonstrated in the Chapter 3, near-field of z component does not contribute to

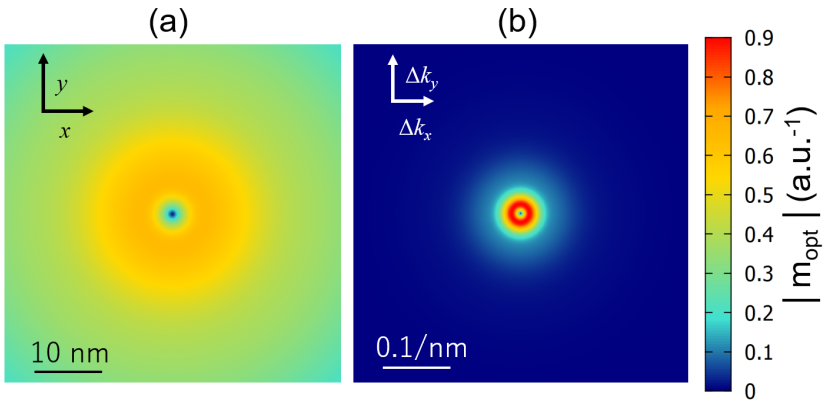

Figure 4.1 Calculated magnitude near-field optical matrix element per unit area of graphene in (a) real space (b) Δk space.

the optical transition of electron in graphene. In the semi-infinite graphene plane, we recognize that the summation over lattice index j in Eq. (4.14) is equivalent the two dimensional Fourier transform. Before we perform the Fourier transform of the near-field optical matrix element given in Eq. (4.16), let us consider the special condition when $\eta_\sigma(\mathbf{R}_j^{\mathrm{u}})$=1, in other words, the magnitude of the electric field is constant everywhere along graphene plane as in the case of far-electric field. Let $m\mathbf{R}_x^{\mathrm{u}} \equiv m(\mathbf{a}_1 + \mathbf{a}_1)/2$ and $n\mathbf{R}_y^{\mathrm{u}} \equiv n(\mathbf{a}_1 - \mathbf{a}_1)/2$, $m, n \in \mathbb{Z}$ define the unit cell position in x and y direction, respectively. Because graphene under consideration is semi-infinite, then the Fourier transform in this case is given by

$$\begin{aligned}
\mathcal{F}[m_{\mathrm{opt}}]_{\Delta\mathbf{k}} &\equiv \frac{1}{N}\sum_j e^{-i\Delta\mathbf{k}\cdot\mathbf{R}_j^{\mathrm{u}}} m_{\mathrm{opt}} \\
&= \frac{1}{N}\sum_n\sum_m e^{-i\Delta\mathbf{k}_x\cdot m\mathbf{R}_x^{\mathrm{u}}} e^{-i\Delta\mathbf{k}_y\cdot n\mathbf{R}_y^{\mathrm{u}}} m_{\mathrm{opt}} \\
&= \frac{1}{(2\pi)^2 N}\int_{-\infty}^{\infty}\mathrm{d}n\int_{-\infty}^{\infty}\mathrm{d}m e^{-i\Delta\mathbf{k}_x\cdot m\mathbf{R}_x^{\mathrm{u}}} e^{-i\Delta\mathbf{k}_y\cdot n\mathbf{R}_y^{\mathrm{u}}} m_{\mathrm{opt}} \\
&= \frac{1}{N_c A_c}\delta(\Delta\mathbf{k}_x)\delta(\Delta\mathbf{k}_y) m_{\mathrm{opt}},
\end{aligned} \tag{4.18}$$

where N_c and $A_c = 3\sqrt{3}a^2/2$ are the number and area of unit cell, respectively. The expression in Eq. (4.18) has non-zero value if only $\Delta\mathbf{k}_x = \Delta\mathbf{k}_y = 0$, which mean when the small momentum of photon is neglected, only vertical transition is possible in the far-field spectroscopy, where there is no change of electron wave vector. On the other hand, in the case of near-field optical transition, the Fourier transform

is performed on the planar components of near-field enhancement $\eta_{\sigma=x,y}(m\mathbf{R}_x^{\mathrm{u}}, n\mathbf{R}_y^{\mathrm{u}})$ given by Eqs. (3.7)-(3.8). The corresponding Fourier transform provides the magnitude of near-field optical matrix element as the function $\Delta\mathbf{k} = (\Delta k_x, \Delta k_y)$ as follows:

$$m_{\mathrm{opt}}^{x}(\Delta\mathbf{k}) = \frac{\Delta k_x}{2\pi N_c A_c}\left(- i\sum_{c=1} C_c f_c^4 e^{\frac{-\Delta k_x^2 - \Delta k_y^2}{2f_c^2}} + \sum_{d=1} D_d g_d^4 e^{\frac{-\Delta k_x^2 - \Delta k_y^2}{2g_d^2}}\right), \tag{4.19}$$

$$m_{\mathrm{opt}}^{y}(\Delta\mathbf{k}) = \frac{\Delta k_y}{2\pi N_c A_c}\left(- i\sum_{c=1} C_c f_c^4 e^{\frac{-\Delta k_x^2 - \Delta k_y^2}{2f_c^2}} + \sum_{d=1} D_d g_d^4 e^{\frac{-\Delta k_x^2 - \Delta k_y^2}{2g_d^2}}\right). \tag{4.20}$$

From Eqs. (4.19) and (4.20), it is inferred that the localization of near-field on the graphene plane imposes a new optical transition rule which exclude the vertical transition that must be satisfied in far-field case, because at $\Delta\mathbf{k}$=0, the near-field optical matrix element is completely zero. Interestingly, the real parts of the near-field distribution contributes to the imaginary part of the optical matrix element, and vice versa. Thus, in our case, the electron-near-field matrix element is a complex number, in contrast with the electron-photon matrix element for the far-field case which is always real, as given by Eqs. (2.98)-(2.100). The magnitude of near-field optical matrix element in real and Δk-space are given by Fig. 4.1(a) and (b), respectively. It is observed that in the case of tip radius a=10 nm, the magnitude of near-field optical matrix element is maximum at $|\Delta\mathbf{k}|$=0.03/nm. It is also important to note that the magnitude of optical matrix element in Δk-space is larger compared with the case of in real-space, mathematically due to the Fourier transform of the optical matrix element.

4.0.2 Effect of Tip radius on the Near-field optical matrix element

For a given excitation wavelength λ ~534 nm, we calculate the near-field optical matrix element as we vary tip radius a. The calculations are performed to provide a clearer picture of how the the distribution of the near-field on graphene affects the properties of optical matrix element. The calculated optical matrix elements in real and Δk-space for tip radius a=5 and 10 nm are given by Fig. 4.2 (a) and (b), respectively. From the figure, it is inferred that because for the smaller tip radius the near-field is more localized, then the width between the peaks of matrix element in the real space is narrower compared with the case of larger tip. However, the narrower width of the the near-field distribution in the real space implies the broader width in the Δk-space,

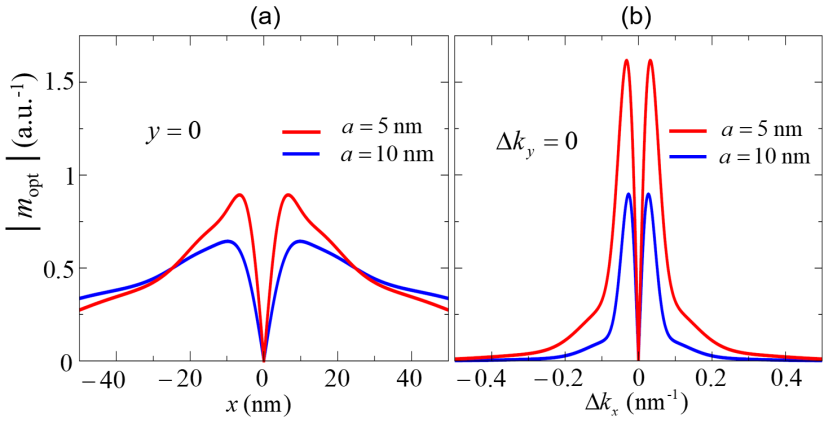

Figure 4.2 Calculated magnitude near-field optical matrix element (a) real space (b) Δk space for a=5 and 10 nm.

which means that the probability of the change of electron wave vector during the optical transition is greater.

4.0.3 Near-Field Transition Probability

In this section, we calculate the transition probability of electron of graphene affected by near-field. We shall not use the transition probability formula in Eq. (2.104) for near-field case because the occurrence of non-vertical optical transition and the direction of near-field can not be described by constant polarization vector **P**. However, based on the same general principle of the Fermi golden rule, the near-field transition probability is given by

$$W_{\mathrm{v}\to\mathrm{c}}(\mathbf{k}_f) = \frac{2\pi}{\hbar}|M_{\mathrm{e-nf}}(\mathbf{k}_i, \mathbf{k}_f)|^2 \delta(\epsilon_{\mathrm{c}}(\mathbf{k}_f) - \epsilon_{\mathrm{v}}(\mathbf{k}_i) - \epsilon_{\mathrm{L}}). \tag{4.21}$$

The calculation is carried out for laser energy $\epsilon_{\mathrm{L}} = 2.32$ eV ($\lambda \sim$534 nm) by using Eq. 4.21. To capture the effect of $\Delta\mathbf{k}_x$ and $\Delta\mathbf{k}_y$ on the transition probability $W_{\mathrm{v}\to\mathrm{c}}(\mathbf{k}_f)$, we plot the values of corresponding variable as a function of several combinations of $\Delta\mathbf{k}_x$ and $\Delta\mathbf{k}_y$, shown By Fig. 4.3. From the figure, it is observed that the change of electron wave vector in x (y) direction will form nodes at $\varphi = 0, \pi, 2\pi$.. ($\varphi = \pi/2, 3\pi/2, ...$). Therefore, we infer an important difference compared with the case of far-field, in which the nodes are determined by the polarization vector **P**, as

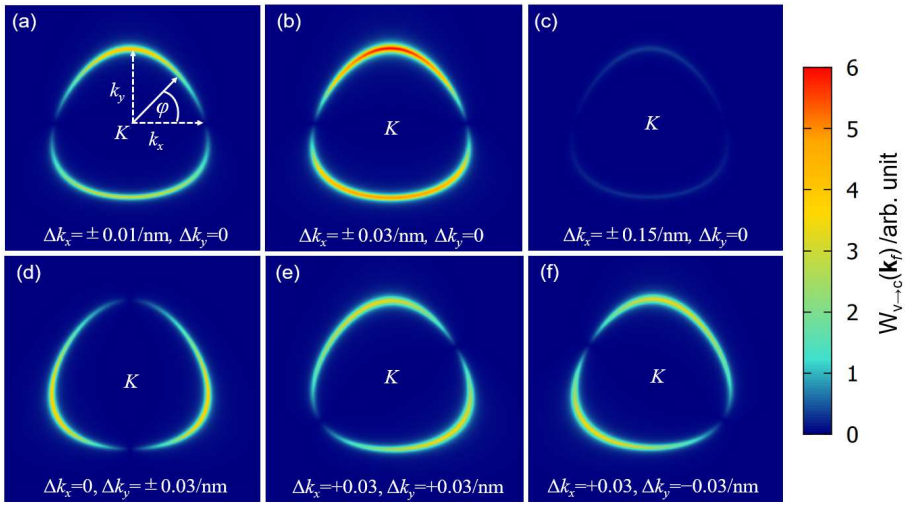

Figure 4.3 Transition probability in the near-field for (a)$(\Delta\mathbf{k}_x, \Delta\mathbf{k}_y) = (\pm 0.01/\text{nm}, 0)$, (b) $(\Delta\mathbf{k}_x, \Delta\mathbf{k}_y) = (\pm 0.03/\text{nm}, 0)$, (b) $(\Delta\mathbf{k}_x, \Delta\mathbf{k}_y) = (\pm 0.2/\text{nm}, 0)$, and (d) $(\Delta\mathbf{k}_x, \Delta\mathbf{k}_y) = (0, \pm 0.03/\text{nm})$, (e)$(\Delta\mathbf{k}_x, \Delta\mathbf{k}_y) = (+0.03/\text{nm}, 0.03/\text{nm})$, and (e)$(\Delta\mathbf{k}_x, \Delta\mathbf{k}_y) = (+0.03/\text{nm}, -0.03/\text{nm})$.

given by Fig. 2.10. From the same comparison, it is also concluded that the transition probability in the near-field case is significantly enhanced.

Finally, it is noteworthy to compare our work very recent results obtained by Mueller and Reich [42], as has been briefly reviewed in Chapter 1. Although utilizing rather different theoretical method, they obtained the some similar results as contained in this thesis, among others the occurrence of non-vertical transition in electron optical transition and the $\Delta\mathbf{k}$-dependence of the transition probability in the case of graphene interaction with the near-field from periodic of plasmonic lattice. However, we have demonstrated that the described phenomena can occur solely due to the localization of near-field on the periodic graphene plane. Therefore, the two studies seem to complement each other.

Chapter 5

Conclusions

Within this thesis, we have performed the quasi-static finite-difference calculation of near-field enhancement around the vicinity of metallic tip as a response of irradiating light. We have shown that for Au tip, the maximum enhancement is obtained for the optical wavelength λ ~534 nm. We also found that the geometrical parameter of the tip plays significant role in determining the maximum magnitude of near-field enhancement factor, that is, the near-field enhancement around the conical tip with the opening angle $\varphi = 15$ degree is higher compared with the case of parabolic tip. The localized near-field in the vicinity of conical tip is further enhanced by selecting the narrow opening angle as well as decreasing the tip radius. We argue that this effect is direct consequence of the electrostatic lightning-rod effect, in which the concentration of electric charge near the tip apex generates the enhanced and localized near-electric field.

After performing the near-field calculation, we investigate the near-field effect on the optical transition of electron in graphene. By using the the tight-binding description of graphene wave function, we analytically demonstrate that the near-field localization along graphene plane produce a new transition rule in which dictates the change of electron wave vector in the transition. We also calculate the electron-near-field optical matrix element, which shows that its magnitude is proportional to the near-field enhancement. What missing is the calculation of electron-phonon matrix element which will enable us to calculate the enhanced Raman spectra in TERS of graphene. This task is considered for the future work.

Appendix A

Calculation Programs

Here we provide programs utilized for the numerical calculations and plottings in this thesis.

The finite-difference method for calculating near-field enhancement based on the quasi-static approximation as the function of incoming electric field from the light E_0 and relative permittivity of $\epsilon(i,k)$ in the case of **parabolic tip** can be found in the FLEX workstation, described as follows:

```
~pratama/for/tip_enhancement/parabola

Program : gfdm1.f90

Inputs : E0, epsilon(i,k)

Outputs : x(i), z(k), V(i,k) or E(i,k)
```

The finite-difference method for calculating near-field enhancement based on the quasi-static approximation as the function of incoming electric field from the light E_0 and relative permittivity of $\epsilon(i,k)$ in the case of **conical tip** can be found in the FLEX workstation described, as follows:

```
~pratama/for/tip_enhancement/parabola

Program : gfdm4.f90

Inputs : E0, epsilon(i,k), a, phi
```

```
Outputs : x(i), z(k), V(i,k) or E(i,k)
```

In both programs, the 1000×1300 square meshes are utilized, in which the area of an individual mesh is 0.1 nm×0.1 nm, as given in Chapter 3 of this thesis. For the corresponding mesh size, the iteration number n required in the algorithm to obtain the electrostatic potential $V(i,k)$ is set as $n = 25000$.

The directory and program for plotting the optical matrix element in the real space due to the near-field enhancement from parabolic tip is given as follows:

The values of Gaussian fitting parameters for tip radius a=5 nm and a=10 nm utilized in this thesis can be found in the following program

```
~pratama/for/tip_enhancement/parabola/matrix element

Program : gaussian_r.f90

Output : x(i), y(j), matrix(i,j)
```

The directory and program for plotting the optical matrix element in the $\Delta\mathbf{k}$-space due to the near-field enhancement from parabolic tip is given as follows:

```
~pratama/for/tip_enhancement/parabola/matrix element

Program : gaussian_k.f90

Output : kx(i), ky(j), matrix(i,j)
```

The directory and program for plotting the transition probability of electron in the Brillouin zone due to the near-field enhancement from parabolic tip as the function change of electron wave vector Δk_x and Δk_x is given as follows:

```
~pratama/for/tip_enhancement/parabola/matrix element

Program : absorption.f90

Input : dkx, dky

Outputs : kx(i), ky(j), Absorption(i,j)
```

Publication List

Conferences

Oral Presentations

1. **F.R. Pratama**, M.S. Ukhtary, and R. Saito: Simulation and principle of tip-enhanced Raman spectroscopy of graphene. Presented in ATI Zao-meeting, (August 9-10, 2017), Zao-Yamagata, Japan.

2. **F.R. Pratama**, M.S. Ukhtary, and R. Saito: Optical transition mechanism in tip-enhanced Raman spectroscopy of monolayer graphene. Presented in ATI Zao-meeting, (August 1-2, 2018), Zao-Yamagata, Japan.

Poster Presentations

1. **F.R. Pratama**, M.S. Ukhtary, and R. Saito: Near field electron-photon matrix element of monolayer graphene. Presented in The 54th Fullerenes-Nanotubes General Symposium (March 10-12, 2017), University of Tokyo, Tokyo, Japan.

Bibliography

[1] R. Saito, M. Hofmann, G. Dresselhaus, A. Jorio, and M.S. Dresselhaus, Advances in Physics 60(3), 413–550 (2011).

[2] M.A. Pimenta, G. Dresselhaus, M.S. Dresselhaus, L.G. Cançado, A. Jorio, and R. Saito, Physical Chemistry Chemical Physics 9(11), 1276–1290 (2007).

[3] A.C. Ferrari and D.M. Basko, Nature nanotechnology 8(4), 235 (2013).

[4] A.C. Ferrari, Solid state communications 143(1-2), 47–57 (2007).

[5] L.M. Malard, M.A. Pimenta, G. Dresselhaus, and M.S. Dresselhaus, Physics Reports 473(5-6), 51–87 (2009).

[6] E. Le Ru and P. Etchegoin, Principles of Surface-Enhanced Raman Spectroscopy: and related plasmonic effects (Elsevier, Oxford, 2008).

[7] A. Cançado, L.G.and Hartschuh and L. Novotny, Journal of Raman Spectroscopy 40(10), 1420–1426 (2009).

[8] Z. Zhang, S. Sheng, R. Wang, and M. Sun, Analytical Chemistry 88(19), 9328–9346 (2016).

[9] P. Verma, Chemical Reviews 117(9), 6447–6466 (2017).

[10] F. Schedin, E. Lidorikis, A. Lombardo, V.G. Kravets, A. K. Geim, A. N Grigorenko, K. S. Novoselov, and A. C. Ferrari, ACS nano 4(10), 5617–5626 (2010).

[11] R. Beams, L. G. Cançado, A. Jorio, A. N. Vamivakas, and L. Novotny, Nanotechnology 26(17), 175702 (2015).

[12] R. Beams, Journal of Raman Spectroscopy 49(1), 157–167 (2018).

[13] R. V. Maximiano, R. Beams, L. Novotny, A. Jorio, and L. G. Cançado, Physical Review B 85(23), 235434 (2012).

[14] F. Frezza, F. Mangini, and N. Tedeschi, JOSA A 35(1), 163–173 (2018).

[15] J. D. Jackson, Classical electrodynamics (Wiley, Hoboken, 1999).

[16] S. A. Maier, , New York, 2007).

[17] V. Amendola, R. Pilot, M. Frasconi, O. M. Maragò, and M. A. Iatì, Journal of Physics: Condensed Matter 29(20), 203002 (2017).

[18] L. Novotny and B. Hecht, Principles of nano-optics (Cambridge university press, Cambridge, 2012).

[19] D. Sarid and W. Challener, Modern introduction to surface plasmons: theory, Mathematica modeling, and applications (Cambridge University Press, Cambridge, 2010).

[20] M. L. Brongersma and P. G. Kik, Surface plasmon nanophotonics (Springer, Dordrecht, 2007).

[21] K. L. Kelly, E. Coronado, L.L. Zhao, and G. C. Schatz. The optical properties of metal nanoparticles: the influence of size, shape, and dielectric environment, 2003.

[22] L. Novotny, R.X. Bian, and X. S. Xie, Physical Review Letters 79(4), 645 (1997).

[23] J. Olson, S. Dominguez-Medina, A. Hoggard, L.Y. Wang, W.S. Chang, and S. Link, Chemical Society Reviews 44(1), 40–57 (2015).

[24] N. Anderson, A. Bouhelier, and L. Novotny, Journal of Optics A: Pure and Applied Optics 8(4), S227 (2006).

[25] J. Cui, L. Yang, and Y. Wang, Laser Physics 23(7), 076003 (2013).

[26] S. Thomas, G. Wachter, C. Lemell, J. Burgdörfer, and P. Hommelhoff, New Journal of Physics 17(6), 063010 (2015).

[27] K. S. Novoselov, A.K. Geim, S.V. Morozov, D. Jiang, Y. Zhang, S.V. Dubonos, I.V. Grigorieva, and A.A. Firsov, Science 306(5696), 666–669 (2004).

[28] A.K. Geim and K.S. Novoselov, Nature Materials 6(3), 183 (2007).

[29] K.S. Novoselov, V.I. Fal, L. Colombo, P.R. Gellert, M.G. Schwab, and K. Kim, Nature 490(7419), 192 (2012).

[30] A. C. Neto, F. Guinea, and N.M. Peres, Physics World 19(11), 33 (2006).

[31] A.C. Neto, F. Guinea, Nuno M.R. Peres, K.S. Novoselov, and A.K. Geim, Reviews of Modern Physics 81(1), 109 (2009).

[32] E.Y. Andrei, G. Li, and X. Du, Reports on Progress in Physics 75(5), 056501 (2012).

[33] E.H. Hasdeo. Gate Modulated Raman Spectroscopy of Graphene. PhD thesis, Tohoku University, 2016.

[34] A. Jorio, M.S. Dresselhaus, R. Saito, and G. Dresselhaus. Raman Spectroscopy in Graphene Related Systems. 2011, 2011.

[35] J.B. Wu, M.L. Lin, X. Cong, H.N. Liu, and P.H. Tan, Chemical Society Reviews 47(5), 1822–1873 (2018).

[36] A. Taguchi, J. Yu, P. Verma, and S. Kawata, Nanoscale 7(41), 17424–17433 (2015).

[37] T. Iwasaki, T. Zelai, S. Ye, Y. Tsuchiya, H.M.H. Chong, and H. Mizuta, Carbon 111, 67–73 (2017).

[38] X. Li, Y.i Liu, Z. Zeng, P. Wang, Y. Fang, and L. Zhang, Spectrochimica Acta Part A: Molecular and Biomolecular Spectroscopy 190, 378–382 (2018).

[39] A. Shiotari, T. Kumagai, and M. Wolf, The Journal of Physical Chemistry C 118(22), 11806–11812 (2014).

[40] P. Verma, K. Yamada, H. Watanabe, Y. Inouye, and S. Kawata, Physical Review B 73(4), 045416 (2006).

[41] C. Williams and D. Roy, Journal of Vacuum Science & Technology B: Microelectronics and Nanometer Structures Processing, Measurement, and Phenomena 26(5), 1761–1764 (2008).

[42] N.S. Mueller and S. Reich, Physical Review B 97(23), 235417 (2018).

[43] M. Fox. Optical properties of solids, 2002.

[44] P.B. Johnson and R.W. Christy, Physical review B 6(12), 4370 (1972).

[45] D. Barchiesi and T. Grosges, Journal of Nanophotonics 8(1), 083097 (2014).

[46] A. Alabastri, A. Tuccio, S.and Giugni, A. Toma, C. Liberale, G. Das, F. De Angelis, E. Di Fabrizio, and R.P. Zaccaria, Materials 6(11), 4879–4910 (2013).

[47] D.M. Solis, J.M. Taboada, L. Landesa, J.L. Rodriguez, and F. Obelleiro, Progress In Electromagnetics Research 154, 35–50 (2015).

[48] D. Gall, Journal of Applied Physics 119(8), 085101 (2016).

[49] W.A. Kraus and G.C. Schatz, The Journal of chemical physics 79(12), 6130–6139 (1983).

[50] E.A. Coronado and G.C. Schatz, The Journal of chemical physics 119(7), 3926–3934 (2003).

[51] M. Liu and P. Guyot-Sionnest, The Journal of Physical Chemistry B 108(19), 5882–5888 (2004).

[52] V. Amendola, O.M. Bakr, and F. Stellacci, Plasmonics 5(1), 85–97 (2010).

[53] U. Kreibig and M. Vollmer, Optical properties of metal clusters (Springer Science & Business Media, Berlin, 2013), Vol. 25.

[54] A. Derkachova, K. Kolwas, and I. Demchenko, Plasmonics 11(3), 941–951 (2016).

[55] L.B. Scaffardi and J.O. Tocho, Nanotechnology 17(5), 1309 (2006).

[56] M.G. Blaber, M.D. Arnold, and M.J. Ford, The Journal of Physical Chemistry C 113(8), 3041–3045 (2009).

[57] J. Larsson, American Journal of Physics 75(3), 230–239 (2007).

[58] N. Behr and M.B. Raschke, The Journal of Physical Chemistry C 112(10), 3766–3773 (2008).

[59] A.E. DePrince and R.J. Hinde, Nanoscale research letters 5(3), 592 (2010).

[60] F. Demming, J. Jersch, K. Dickmann, and P.I. Geshev, Applied Physics B 66(5), 593–598 (1998).

[61] J.R. Nagel. Solving the generalized poisson equation using the finite-difference method (fdm), 2012.

[62] M. Hjorth-Jensen. Computational physics, 2011.

[63] D.A. Genov, A.K. Sarychev, V.M. Shalaev, and A. Wei, Nano Letters 4(1), 153–158 (2004).

[64] A.K. Sarychev and V.M. Shalaev, Electrodynamics of metamaterials (World Scientific, Singapore, 2007).

[65] A.S. McLeod, P. Kelly, M.D. Goldflam, Z. Gainsforth, A.J. Westphal, G. Dominguez, M.H. Thiemens, M.M. Fogler, and D.N. Basov, Physical Review B 90(8), 085136 (2014).

[66] C. Sönnichsen, T. Franzl, T. Wilk, G. von Plessen, J. Feldmann, O.V. Wilson, and P. Mulvaney, Physical review letters 88(7), 077402 (2002).

[67] A. Grüneis. Resonance Raman spectroscopy of single wall carbon nanotubes. PhD thesis, Tohoku University, 2004.

[68] A. Grüneis, R. Saito, G.G. Samsonidze, T. Kimura, M.A. Pimenta, A. Jorio, A.G. Souza Filho, G. Dresselhaus, and M.S. Dresselhaus, Physical Review B 67(16), 165402 (2003).

[69] A. Vial, A.S. Grimault, D. Macías, D. Barchiesi, and M.L. de La Chapelle, Physical Review B 71(8), 085416 (2005).